Characterization, Optimization, and Operation of TES Bolometers for EBEX

A DISSERTATION
SUBMITTED TO THE FACULTY OF THE GRADUATE SCHOOL
OF THE UNIVERSITY OF MINNESOTA
BY

Catherine Raach

IN PARTIAL FULFILLMENT OF THE REQUIREMENTS
FOR THE DEGREE OF
Doctor of Philosophy

SHAUL HANANY

April, 2018

Acknowledgements

My deepest gratitude goes to those who have supported me in my journey. Though I may have taken the lifelong cosmolab membership a little too literally, this thesis is finally out of my hands.

Thank you to the NASA EBEX grant and to the NASA MN Space Grant for their generous support of this research.

Dedication

To Alexandra Marie. Sorry, babe.

Abstract

The cosmic microwave background (CMB) radiation holds a wealth of information about the evolution of the universe. In particular, measurement of the B-mode polarization pattern of the CMB is a direct probe of the physics of inflation. The E and B Experiment (EBEX) was a balloon-borne telescope designed to search for inflation's signature on the polarization of the CMB. To achieve the high receiver sensitivity necessary to measure a small polarization signal, I assembled, tested, and integrated a kilopixel array of transition edge sensor bolometers. I worked with the fabrication team at UC Berkeley to modify and optimize the bolometer design for the space-like environment at a float altitude of 36 km. The detector characterization measurements, I performed in test cryostats and in EBEX itself, are reported here. I measured the bolometer normal resistances, thermal conductances, critical temperatures, optical efficiencies, time constants, and noise equivalent powers. I also report on the detector performance, with a particular focus on sensitivity and noise, from the 2013 Antarctic flight.

Contents

List of Tables

List of Figures

Chapter 1

Introduction

1.1 Cosmic Microwave Background Polarization

We seek to answer a fundamental question in cosmology: how did the universe we know today (the galaxies, the stars, and the planets) come about? Merely 10^{-34} seconds after the big bang, the universe underwent a period of exponentially accelerated expansion, an epoch called inflation [1] [2] [3] [4] [5] [6] [7]. 380,000 years later, the universe became transparent to light when the baryon-photon plasma cooled enough for neutral hydrogen to form. Those photons, the oldest light in the universe, are called the cosmic microwave background (CMB). The scalar primordial energy density perturbations imprinted a curl-free, or 'E-mode', polarization pattern on the CMB. The E-mode polarization is at a level of 1 μK and has been measured by several groups [8] [9] [10] [11] [12].

Inflation predicts the existence of a tensor stochastic background of gravitational waves which also left a curl component, or 'B-mode', in the polarization of the CMB. The energy scale of inflation is proportional to the amplitude of this tensor B-mode polarization and it depends on the mechanism which drove the rapid acceleration [13] [14] [15] [16] [17]. Detection of the tensor B-mode polarization (or placing a constraint of 0.001 on the tensor to scalar ratio, r) is important because it would confirm (or rule out) the single field slow-roll inflation model [18]. Across the sky, the polarized thermal emission from galactic dust is the largest foreground above 100 GHz [19] and will need to be subtracted in order to extract the tensor B-mode signal from the CMB. There is also a B-mode polarization pattern in the CMB, at smaller angular scale, due to

gravitational lensing of the E-mode polarization [20] [21] [22]. Figure 1.1 shows the predicted E- and B-mode polarization power spectra of the CMB as a function of l. The prediction assumes the ΛCDM model and takes r to be 0.05, which is slightly below the current upper limit set by the Planck and Keck Array joint analysis [23].

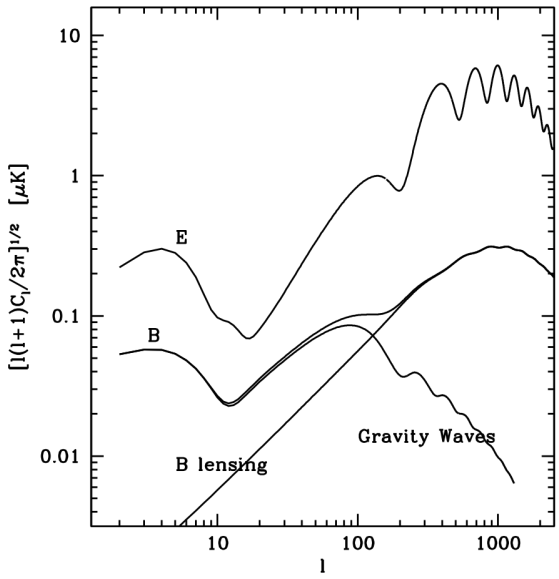

Figure 1.1: The theoretical prediction of the E- and B-mode power spectra of the CMB. The E-mode polarization has been measured to high accuracy. The B-mode power spectra is expected to have a component due to lensing, which has been measured, and a component due to primordial gravity waves, which hasn't yet been detected with high confidence. This plot shows the level of the B-mode polarization assuming a tensor-to-scalar ratio of r=0.05.

1.2 High-Altitude Ballooning

High-altitude balloons, relative to satellites, are powerful platforms for achieving low budget and fast astrophysical studies. The high altitude observation environment also enables measurement of frequencies inaccessible on the ground. The high frequency data are critical to determine the spectra of dust so the dust foreground can be subtracted from the signal.

One challenge in ballooning is the length of observation. Figure 1.2 shows the E and B Experiment (EBEX) flight path. The average long duration balloon (LDB) flight duration from McMurdo, Antarctica is 18 days, and the longest flights have lasted more than 40 days. While this is much shorter than the operation time of a ground-based telescope, the factor of $\sim$3 increase in instantaneous detector sensitivity in the space-like environment can make a high-altitude balloon experiment worthwhile. Section 2.2 discusses the detector design modifications we performed to optimize the detector sensitivity for a space-like environment. The typical flight altitude is around 36 km, above approximately 98% of the atmosphere. At this altitude, and at an elevation of 45°, the radiative load from the atmosphere is less than 0.04 pW for the 150 and 250 GHz observation bands and around 2 pW for the 410 GHz observation band [24].

Antarctic flights offer the longest flights on the planet with the highest probability of data recovery. Favorable wind patterns set up in the austral summer to bring the balloon around in a circle, usually staying over the continent, and coming back to roughly where it began, see Figure 1.2. The continent is sparsely populated so there is little danger of injuring anyone or anything. Also, during the austral summer in Antarctica, the payloads are exposed to the sun around the clock. The batteries need to provide just enough power to make it through launch and ascent and then the sun exposure allows for constant charging of the solar panels to power the experiment. This is important for minimizing the weight of the payload.

1.3 The E and B EXperiment

EBEX was a balloon-borne telescope flown on an Antarctic long duration balloon flight supported by National Aeronautics and Space Administration (NASA)'s Columbia Scientific Balloon Facility (CSBF). EBEX was designed to measure the polarization of the CMB. The goals of the project were to:

- measure or put an upper limit on the B-mode polarization signal due to primordial gravitational waves
- measure the polarization of the galactic foregrounds, in particular galactic dust
- measure the B-mode polarization signal due to lensing and effectively separate it

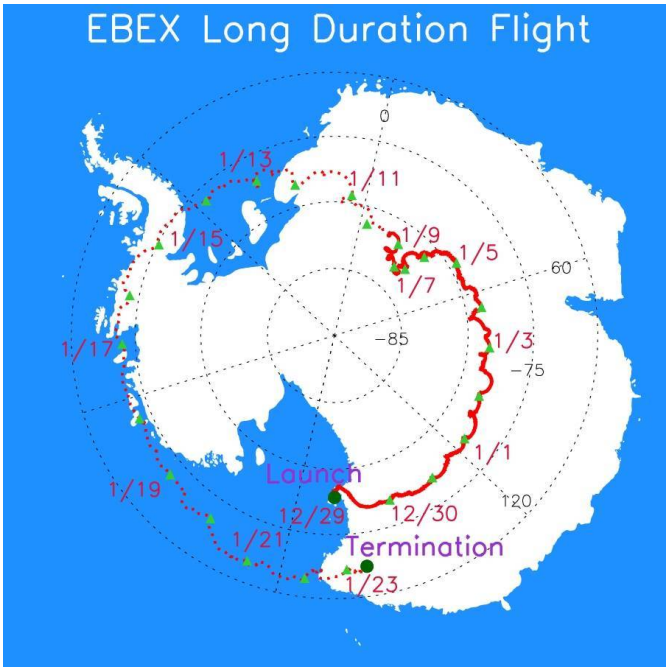

Figure 1.2: The flight path EBEX followed over Antarctica. On January 9, the trajectory line goes from solid to dashed because, exactly as predicted, the liquid helium ran out after twelve days and so EBEX stopped collecting data.

from the signal due to gravity waves

- measure the E-mode polarization signal
- provide a milestone in the implementation and testing of detectors, detector readout, optics, and polarimetry techniques being considered for a future NASA CMB polarization satellite

This thesis contributes to the final item, in particular, the implementation and testing of the detectors and their readout.

EBEX had three observation frequency bands, designed to be centered around 150, 250, and 410 GHz. The lowest frequency band was the CMB observation band. The higher frequency bands were included to measure the polarization of the galactic dust so it could be accurately subtracted from the CMB observation band. Foreground subtraction was predicted to be necessary because, even in the planned observation clean sky patch of $\sim$400 deg^2, the dust was predicted to dominate the primordial gravitational B-mode signal [24].

EBEX was an off-axis Gregorian telescope. The outer frame carried the pointing control, the experiment power, and the flight control computer. The inner frame carried the 1.5 m primary mirror, the 1 m secondary mirror, the cryostat, and the readout electronics. The left panel of Figure 1.3 is a model of EBEX and the right panel is the instrument in a similar configuration to the model, but is a photograph of it hanging on the launch pad [25]. The majority of the telescope was surrounded by mylar-covered baffling protecting it from the light of the sun. The solar panels were mounted to the back of the telescope to be constantly charging while the telescope front was set to point anti-sun.

The path of light through the telescope is shown in Figure 1.4. Light bounced off the primary mirror and was reflected into the cryostat by the secondary mirror. The light entered the cryostat via an ultra-high molecular weight polyethylene (UHMWPE) 1.0 mm window, transparent to mm-wave light. On the ground, this window under vacuum would have deflected enough to damage the filters beneath it. To prevent that from happening, the telescope had a double window mechanism mounted to the top of the cryostat, Figure 1.5 [27]. On the ground, there was an additional UHMWPE window of thickness 12.7 mm under vacuum above the thin window. At float, the thick

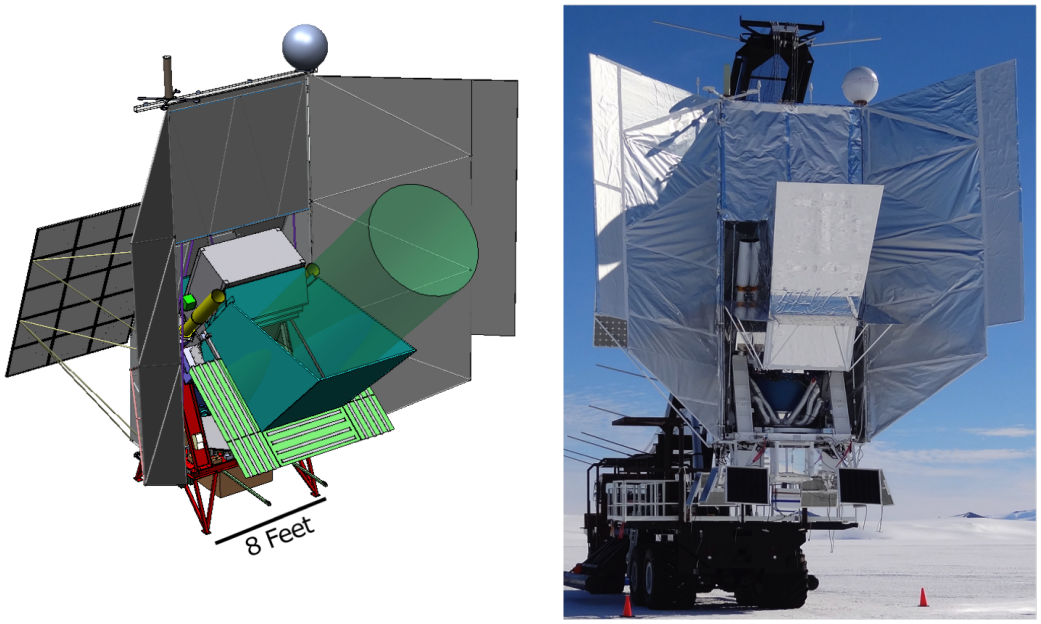

Figure 1.3: Left: Model of EBEX [26]. There is a green cylinder showing the path of light entering the telescope via the teal scoop. Neon green radiation panels, to dissipate power from the readout electronics at float, surround the scoop. The solid grey panels are the mylar-covered baffling. Attached to the rear, a single solar panel is visible as a black grid on a grey rectangle. Right: Photograph of EBEX hanging on the launch vehicle in Antarctica. Photograph courtesy of Asad Aboobaker.

window was rolled back. Once the light entered the cryostat, it was filtered and passed through a half-wave plate continuously rotating at 1.235 Hz. There was a polarizing grid through which half of the light passed and was focused onto the horizontal focal plane. The other half of the light reflected off of the polarizing grid and was focused onto the vertical focal plane. Figure 1.6 shows a model of the interior of the cryostat and a photograph of the optical elements housed inside the optics box [28].

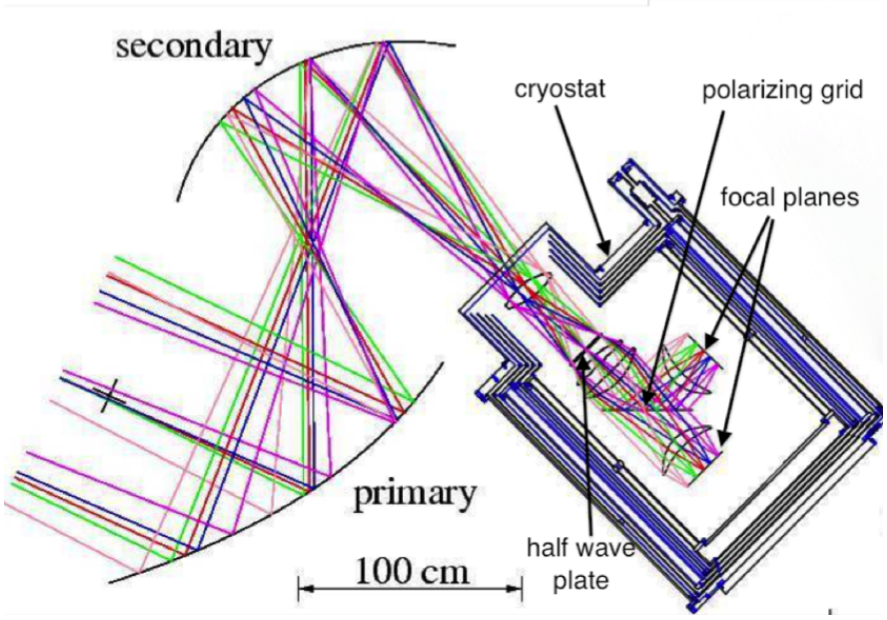

Figure 1.4: Path of light, the multicolored bundle of rays, through EBEX. It first strikes the primary mirror, is reflected onto the secondary mirror, passes through the cryostat window, and is focused onto the cold aperture stop where the half-wave plate is mounted. From there it is imaged onto the two focal planes.

There were two focal planes and each focal plane consisted of seven silicon wafers of detectors, four at 150 GHz, two at 250 GHz, and one at 410 GHz, see Figure 1.7 [29]. Each wafer had 140 detectors fabricated via thin metal deposition and optical lithography. See section 4.1 for a discussion of the detector yield achieved. Each wafer was mounted to an invar plate with a thin layer of warmed Apiezon N grease. The invar plate was screwed to an aluminum wafer/LC board mount and an alignment jig was used to position the wafer relative to dowel pin holes on the waveguide array. The

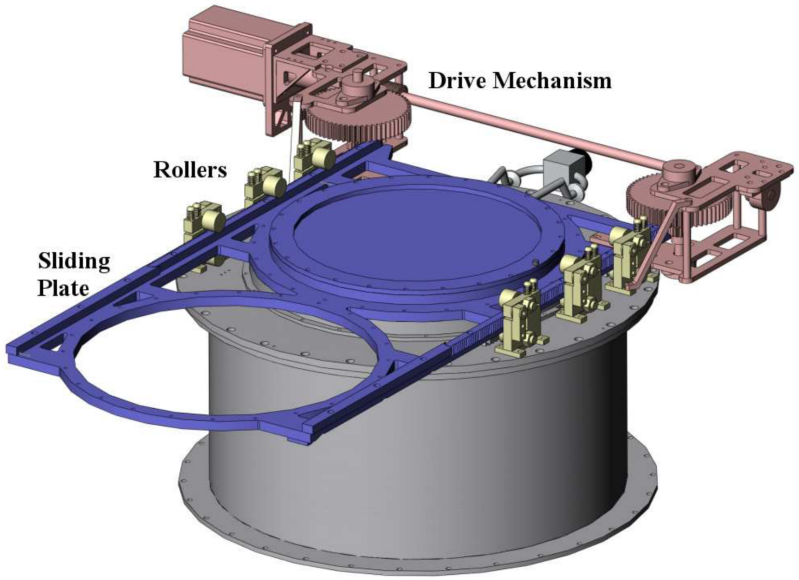

Figure 1.5: The EBEX double window design. On the ground, there were two windows under vacuum. At float, the thick 12.7 mm window was rolled back and only the thin 1.0 mm window remained in the light path. [26]

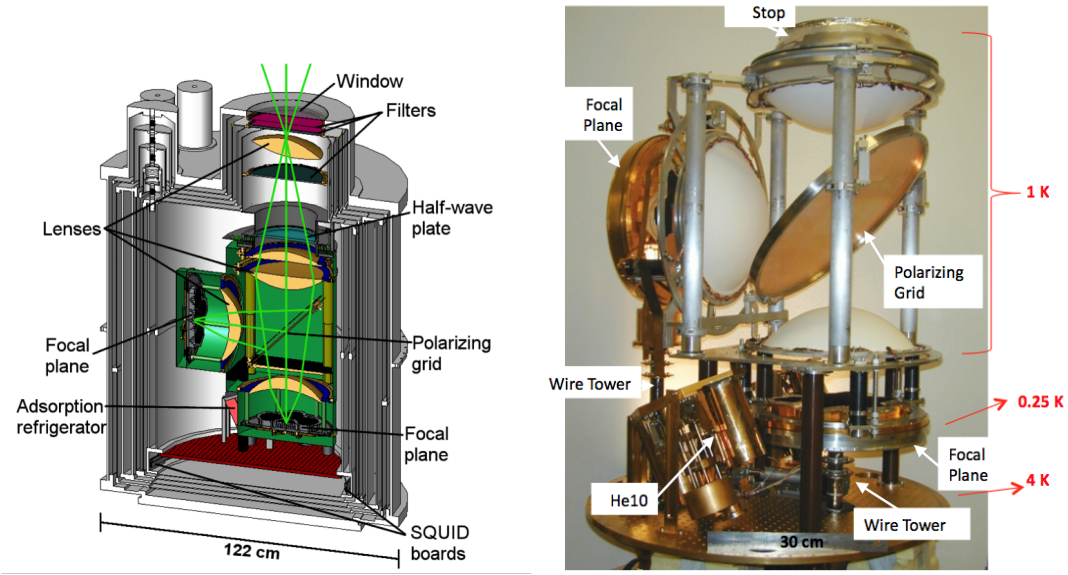

Figure 1.6: Left: Cross-section of EBEX cryostat model. The grey shells are the toroidal cryogen tanks and vapor cooled shells. Light is represented as neon green rays. The light passes through the window, the filter stack, the continuously rotating half-wave plate, lenses, and is split at the polarizing grid. Half of the photons continue to the horizontally mounted focal plane below and the other half are reflected to the vertically mounted focal plane to the side. Right: Photograph of EBEX cold plate and optics elements beneath the half-wave plate. The half-wave plate sits above the stop at the top of the stack shown. The orange circle at a 45° angle is the polarizing grid. The focal planes are the gold plated enclosures with the wiring towers beneath them. The structures are supported by thin walled vespel legs. One of the Simon Chase helium adsorption refrigerators is visible mounted to the cold plate on the lower left of the photograph.

invar plates were heat sunk to a Simon Chase helium adsorption fridge which cooled the wafers to ∼250 mK.

The detector signals were read out using digital frequency domain multiplexer (DfMUX) electronics, Figure 1.8. The detectors were nominally grouped into combs of sixteen detectors per pair of wires leading from the focal plane. Each detector was wired in series with a 24 uH inductor and ceramic capacitor between ∼0.9 and 30 nF on the LC board. This gave a comb of sixteen resonant frequencies from 200 to 1200 kHz, with spacing of roughly 65 kHz. The signal from each comb was amplified by a NIST 100 series array superconducting quantum interference device (SQUID). The DfMUX carriers, and a 0.03 Ω resistor, provided each detector's voltage bias at its resonant frequency and the DfMUX nullers canceled the bias signal at the input of the SQUID. To bring the comb of signals from the 250 mK LC boards to the 4 K SQUIDs, there was a short pair of kapton encased flattened copper wires attached to a pair of low-inductance parallel kapton encased flattened niobium titanium wires. A twisted pair of 150 mm long manganin wire exited the cryostat carrying the signal from the 4 K squids to the room temperature SQUID controller board. The DfMUX board demodulated the signal and the flight control computer recorded all of the data.

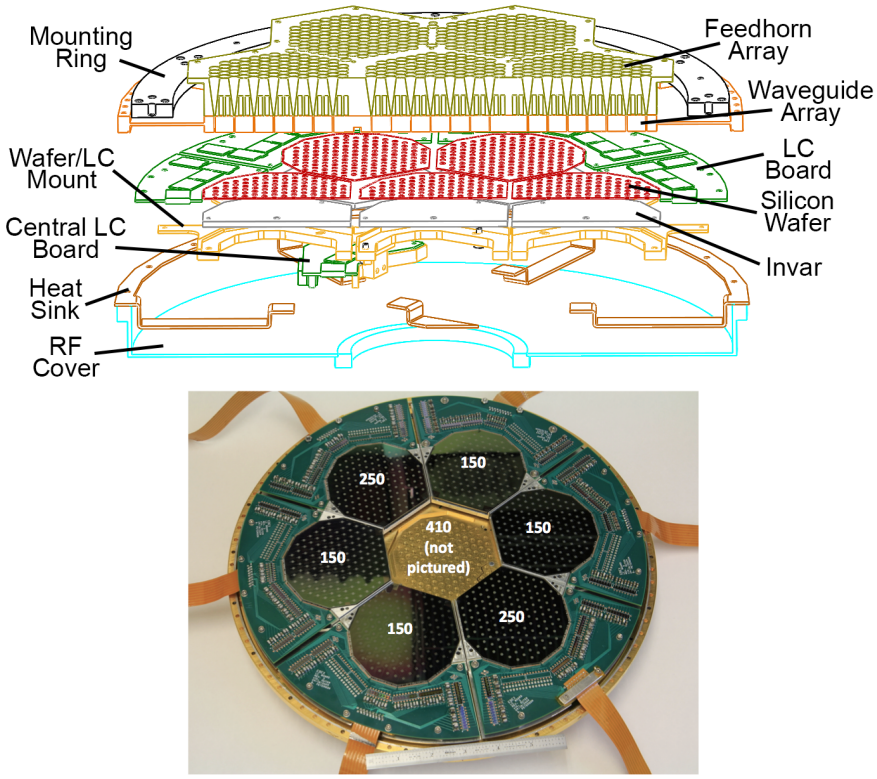

Figure 1.7: Top: An exploded model of the focal plane. Light passes through low pass filters (not pictured), to the feedhorns and waveguides, to the bolometers in their integrating cavities below. Each wafer is mounted to an invar plate which is attached to an aluminum wafer/LC mount. The wafer is wirebonded to an LC board. Note, the central LC board is offset into the space behind the wafer/LC mounts. There is a copper heat sink ring around the perimeter and attaching to each invar plate. The entire assembly is enclosed by an RF cover. Bottom: The silicon detector wafers wirebonded to their LC boards. The wafer assemblies are sitting atop the gold-plated waveguide and horn array. The copper pigtails are leading off the edge of the photograph, but when fully assembled are routed through the wiring towers. The 410 GHz wafer with its offset LC board is not included in the photograph.

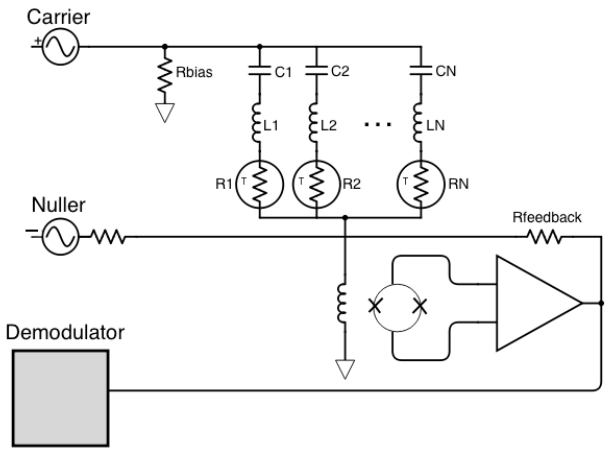

Figure 1.8: Schematic of readout electronics.

Chapter 2

Detector Design and Optimization

EBEX employed a kilopixel array of transition edge sensor (TES) bolometers, described in Section 2.1. These types of detectors were used on ground-based telescopes, like the Atacama Pathfinder Experiment and the South Pole Telescope [30] [31]. We modified the design, described in Section 2.2, in order to optimize the detectors to take advantage of the space-like environment in which EBEX was flown.

2.1 Bolometer Theory

A bolometer, first invented by Langley in the late 1800s, is an absorber with some heat capacity weakly thermally coupled to a bath [32]. Figure 2.1 is a schematic of a bolometer. Bolometers absorb power from radiation, via the heat capacitive element, and measure the resultant change in temperature with a thermistor. The bolometer's steady state power flow, P, from the absorber to the bath is described by

$$P = \overline{G}\,(T - T_{bath}) = \overline{G}\Delta T \tag{2.1}$$

where $\overline{G}$ is the average thermal conductance along the weak link and ΔT is the difference between the absorber and bath temperatures. The dynamic thermal conductance of the weak link is

$$G \equiv \frac{dP}{dT} \tag{2.2}$$

and is a function of position along the link. When additional power is deposited on the bolometer and absorbed, the temperature of the heat capacitive element increases and then the absorbed power dissipates to the bath via the link with a characteristic time constant of

$$\tau = \frac{C}{G} \tag{2.3}$$

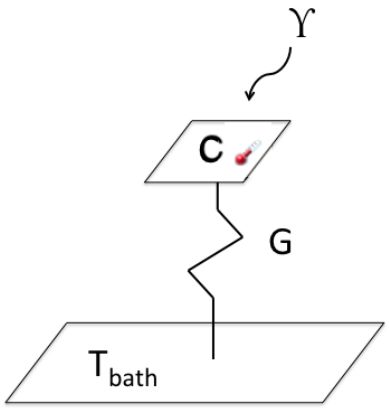

Figure 2.1: Cartoon bolometer with incoming radiation, γ. There is an absorber, with heat capacity C, weakly coupled, with thermal conductance G, to a reservoir at T_{bath}. A thermistor measures the change in temperature due to the power absorbed.

2.1.1 Transition Edge Sensors

A TES bolometer has a superconductor as its thermistor. A superconductor is a special material which has a normal resistance until it drops below its critical temperature, at which point its resistance drops to zero [33]. Figure 2.2 shows the resistance as a function of temperature for a superconductor. The TES is called such because it is a sensor operated on the edge of its superconducting transition, where there is a steep change in resistance as a function of temperature.

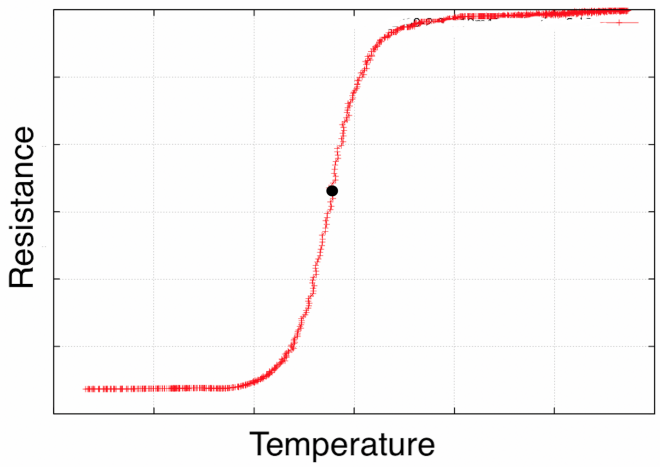

Figure 2.2: Resistance versus temperature for an EBEX TES bolometer. As the temperature goes from high to low, the TES goes from a finite normal resistance to superconducting with zero resistance. The region in between is the transition. The TES is biased roughly in the middle (black dot) for operation.

Negative Electrothermal Feedback

To operate the detector, a voltage bias, V_{bias}, is applied across the TES. The voltage bias provides Joule heating of $P_{elec} = V_{bias}^2/R$, where R is the resistance of the TES. To understand the electrothermal feedback loop, i.e. what happens to the power dissipated in the bolometer when its temperature changes by a small amount, we take the derivative of the electrical power with respect to temperature,

$$\begin{aligned} \frac{dP_{elec}(T)}{dT} &= \frac{-V_{bias}^2}{R^2}\frac{dR}{dT} = -\frac{V_{bias}^2}{R}\frac{T}{R}\frac{dR}{dT}\frac{1}{T} \\ &= -\frac{P_{elec}\alpha}{T} \end{aligned} \tag{2.4}$$

where we define α to be a unitless measure of the slope of the resistance versus temperature curve,

$$\alpha \equiv \frac{d\log R}{d\log T} = \frac{T}{R}\frac{dR}{dT} \tag{2.5}$$

Since the slope of the resistance versus temperature curve is positive for a TES, the change in power is opposite in sign to the change of temperature. This negative electrothermal feedback holds the detector between normal and superconducting, at the

edge of its transition.

Qualitatively, the voltage bias is chosen such that the detector is heated just enough to hold the TES between normal and superconducting. When the radiative load changes, the TES warms (cools). This change in temperature moves the detector up (down) its R vs T curve. In response to the increase (decrease) in resistance, the Joule heating decreases (increases) and the detector cools (warms). For small changes in temperature, this feedback holds the detector at the transition between normal and superconducting. The voltage bias is constant and so the excursions in resistance change the current through the detector and this is what we measure.

Responsivity

To derive the detector responsivity we follow [34] and [35]. The radiative signal absorbed by the detector consists of a steady state power P_0 and a time varying signal of amplitude δP and frequency ω

$$P_{rad} = P_0 + \delta P e^{i\omega t} \tag{2.6}$$

The bolometer temperature is then also a function of time

$$T = T_0 + \delta T e^{i\omega t} \tag{2.7}$$

The total input power is the sum of the electrical power dissipated, P_{elec} (including the first order change in electrical power due to the change in detector temperature), and the radiative power absorbed, P_{rad},

$$P_{in} = P_{elec} + P_{rad} = \frac{V_{bias}^2}{R} - \frac{V_{bias}^2}{R^2}\frac{dR}{dT}\delta T e^{i\omega t} + P_0 + \delta P e^{i\omega t} \tag{2.8}$$

The total output power is the steady state power flow to the bath, Equation 2.1, plus the time varying power to the bath plus the time varying power stored in the heat capacity

$$P_{out} = \overline{G}\Delta T + G\delta T e^{i\omega t} + i\omega C \delta T e^{i\omega t} \tag{2.9}$$

Power is conserved, so Equation 2.8 equals Equation 2.9. The time-independent portion is

$$P_0 + \frac{V_{bias}^2}{R} = \overline{G}\Delta T \tag{2.10}$$

The time-dependent portion is

$$\delta P - \frac{V_{bias}^2}{R^2}\frac{dR}{dT}\delta T = G\delta T + i\omega C\delta T \tag{2.11}$$

It describes the change in power due to a small change in temperature

$$\begin{aligned}\frac{\delta P}{\delta T} &= \frac{V_{bias}^2}{R^2}\frac{dR}{dT} + G + i\omega C \\ &= \frac{P_{elec}\alpha}{T} + G + i\omega C\end{aligned} \tag{2.12}$$

The electrothermal feedback loopgain is the change in electrical power in response to the small absorbed radiative signal relative to the signal amplitude

$$\mathscr{L}(\omega) = -\frac{\delta P_{elec}}{\delta P} = \frac{P_{elec}\alpha}{GT(1+i\omega\tau_0)} = \frac{\mathscr{L}}{1+i\omega\tau_0} \tag{2.13}$$

The DC value of the loopgain is

$$\mathscr{L} = \frac{P_{elec}\alpha}{GT} \tag{2.14}$$

and it rolls off with a time constant of $\tau_0 = C/G$. The current responsivity of the detector is the change in current we measure for a given amount of radiative power absorbed

$$S_I \equiv \frac{\delta I}{\delta P} = -\frac{1}{V_{bias}}\left(\frac{\mathscr{L}}{\mathscr{L}+1}\right)\left(\frac{1}{1+i\omega\tau_{eff}}\right) \tag{2.15}$$

where $\tau_{eff} = \tau_0/(1+\mathscr{L})$ is the effective time constant, sped up by electrothermal feedback. Note, for the DfMUX system, there is an additional factor of $\sqrt{2}$ in the current responsivity due to demodulation.

2.1.2 Noise Equivalent Power

The sensitivity of the detectors is quantified by their noise equivalent power (NEP). NEP is defined as the absorbed power required to produce a signal-to-noise ratio of one in a bandwidth of one Hz. For purposes of brevity, we will also refer to the NEP simply as noise. There are four contributors to the TES bolometer NEP: electronic readout noise, Johnson noise, phonon noise, and photon noise. The total predicted detector NEP, N, is given by

$$N^2 = N_{photon}^2 + N_{phonon}^2 + N_{Johnson}^2 + N_{readout}^2 \tag{2.16}$$

$$= 2h\nu P_{rad} + \xi \frac{P_{rad}^2}{\Delta\nu} + \gamma 4k_B T^2 G + \frac{1}{S_I^2}\left(\frac{4k_B T}{R} + N_{readout}^2\right) \tag{2.17}$$

where h is Planck's constant, ν is the center of the observation frequency band, P_{rad} is the radiative power absorbed by the bolometer, ξ is a unitless number between zero and one quantifying the contribution of photon correlation noise, $\Delta\nu$ is the width of the observation frequency band, γ is a unitless number between zero and one accounting for the temperature gradient along the link from the TES to the bath, k_B is Boltzmann's constant, T is the TES temperature, G is the bolometer dynamic thermal conductance, S_I is the bolometer current responsivity, and R is the TES resistance [36]. TES bolometers have been developed such that the the fundamental limit of the NEP can be set by the photon arrival statistics, i.e. background limited. We wanted to create an instrument with background noise limited TES bolometers.

Readout Noise

The electronic readout noise is due to current and voltage fluctuations in the readout electronics, i.e. the carrier, nuller, and demodulator circuits, schematic shown in Figure 1.8. The electronic components were sourced with the requirement that their noise, added in quadrature, provided a subdominant contribution to the NEP. The largest contributors were the 4.2 K SQUIDs and their room temperature first stage operational amplifiers. Measurements of the electronic and readout noise are discussed in Section 3.2 and Section 4.3.

Johnson Noise

The Johnson noise is due to the thermal agitation of the electrons in the TES. As a voltage-referred noise, in units of V^2/Hz, the Johnson noise power spectral density (PSD) is $4k_BTR$, where k_B is Boltzmann's constant, T the temperature of the resistor, and R the resistance [37]. Note, this voltage noise source is present regardless of any applied voltage. In order to convert the Johnson noise from our TES to a current-referred noise, we divide the voltage noise amplitude spectral density (ASD) by R, $\sqrt{4k_BTR}/R = \sqrt{4k_BT/R}$. For NEP, in order to convert from $A/\sqrt{Hz}$ to $W/\sqrt{Hz}$, we divide the current noise by the bolometer's current responsivity, $S_I = dI/dP$. The

Johnson NEP is thus

$$N_{Johnson} = \frac{1}{S_I}\sqrt{\frac{4k_BT}{R}} \tag{2.18}$$

Phonon Noise

The phonon noise is due to the motion of the thermal carriers, phonons, along the weak thermal link. This random thermodynamic energy flow gives rise to the phonon NEP,

$$N_{phonon} = \sqrt{\gamma 4k_BT^2G} \tag{2.19}$$

where k_B is Boltzmann's constant, T is the temperature of the TES, and $G \equiv dP/dT$ is the dynamic thermal conductance along the weak link [36]. γ is a unitless number between zero and one which describes the temperature gradient along the thermal link from the TES to the bath

$$\gamma \equiv \frac{\int_{T_{bath}}^{T}\left(\frac{t\kappa(t)}{T\kappa(T)}\right)^2 dt}{\int_{T_{bath}}^{T}\frac{\kappa(t)}{\kappa(T)}dt} \tag{2.20}$$

where κ is the thermal conductivity, T is the bolometer temperature, and T_{bath} is the bath temperature [36]. When we assume $\kappa(T) = \kappa_0 T^n$ and also assume the bolometer temperature T is equal to its critical temperature T_c, then

$$\gamma = \frac{n+1}{2n+3}\frac{1-\left(\frac{T_{bath}}{T_c}\right)^{2n+3}}{1-\left(\frac{T_{bath}}{T_c}\right)^{n+1}} \tag{2.21}$$

Photon Noise

The photon noise is due to the particle nature of photons and the statistics which govern their arrival. Quantifying the fluctuations in the absorbed energy (via boson statistics) and integrating over the radiation bandwidth, the photon NEP is

$$N^2_{photon} = 2\int h\nu P_\nu d\nu + \xi\int \frac{P_\nu^2 c^2}{A\Omega\nu^2}d\nu \tag{2.22}$$

where h is Planck's constant, ν is the frequency of the radiation, P_ν is the absorbed spectral power, and ξ is the so-called correlation factor [34]. If we assume the spectral power is roughly constant over a small bandwidth and that we have a diffraction limited beam so the throughput is $A\Omega = \lambda^2$, where Ω is the solid angle of a wave after passing

through a circular aperture of area A and λ is the wavelength of the incident light, then the photon NEP becomes

$$N_{photon} = \sqrt{2h\nu P_{rad} + \xi \frac{P_{rad}^2}{\Delta\nu}} \tag{2.23}$$

where P_{rad} is the radiative power absorbed and $\Delta\nu$ the observation frequency bandwidth.

The first term of the photon NEP is often referred to as shot noise. The second term is only relevant if the photon arrivals are correlated, that is if the photons tend to arrive in bunches. This is called photon correlation or bunching noise. The degree to which this second photon noise term contributes to the bolometer NEP is not agreed upon [34]. This disagreement is encapsulated in the factor of ξ which is multiplied by the noise one would have in the case of complete correlation. ξ can take on a value between zero (no correlation) and one (completely correlated). Lamarre writes, the photon correlation factor when the "beam is produced by an incoherent source and is uniformly distributed over the beam throughput, which is large with respect to the etendue of coherence ν^2/c^2" is completely different than the photon correlation factor in the case of telescopes "observing sources with angular diameters much smaller than the diffraction pattern" [38]. While our source, the CMB, is incoherent and uniformly distributed over the beam throughput, the beam throughput is equal to (so not large with respect to) the etendue of coherence. It is not clear what the true value of ξ should be for EBEX.

2.2 Detector Design

The EBEX bolometers were fabricated on a silicon device wafer, the thickness of which, $\lambda/4$, was determined by the center of the observation band. The device wafer was glued to a thick silicon backing wafer for mechanical stability [39]. The left panel of Figure 2.3 is a photograph of a single EBEX bolometer. The absorber, to which radiation coupled, was a 1 μm thick silicon nitride spider web. The silicon nitride was deposited on the device wafer and a silicon etch carved away the silicon underneath so the web was actually suspended in space. The link to the bath was provided by eight legs which attached the web to the silicon wafer. The heat capacity was provided by a gold waffle,

called bling, in the center. The TES itself was an AlTi bilayer in the shape of a 19 x 19 μm^2 square located towards the center of the bling. The left edge of the bilayer overlapped the bling, right panel of Figure 2.3, providing the thermal coupling between the absorber and the TES.

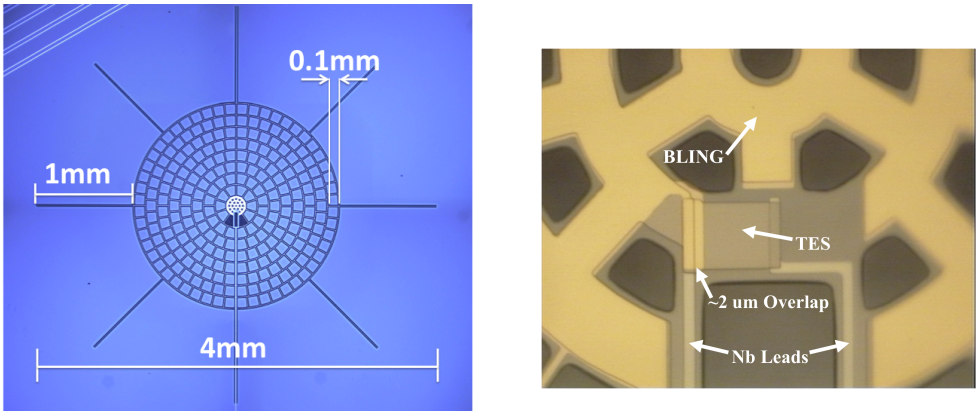

Figure 2.3: Left: One EBEX 150 GHz spiderweb TES bolometer. The light blue is the silicon wafer on which the detectors were fabricated. The dark blue is open space where the silicon was etched away. Running above the center of the etched out area are the thin silicon nitride strings of the spider web. The spider web is attached to the wafer at the end of each of the spokes. The gold waffle bling in the center provides the heat capacity. Right: A zoom of the bling and the TES. The TES is a square near the middle of the bling and is coupled to the bling via the overlap on its left side. The signal travels out the niobium leads to bond pads at the wafer's edge. Both figures courtesy of Benjamin Westbrook.

Normal Resistance

The TES bolometer response would be unstable if it were underdamped or had exponentially increasing oscillations [40]. The goal was to ensure the detector, when biased in the transition, remained in the stable regime. The stability of the detector depended on the value of the normal resistance. In order to be stable, the bolometer's LCR filter bandwidth, $\Delta B = R_{bolo}/(2\pi L)$, needed to exceed the TES' effective thermal bandwidth by a factor of 5.8 [41]. With our inductors of 24 μH and expected thermal time constants on the order of 10 ms, the target normal resistance for all bands was 1.5 Ω, Table 2.2.

The electrical cross-talk was also a function of the bolometer resistance. In designing the electronics, we required the electrical cross-talk be subdominant to the optical cross-talk, due to beam side-lobes and radiation leakage within the detector integration cavity, which is typically at a level of ∼1% [42] . This electrical cross-talk was estimated by Dobbs, et al. [42] to be

$$\left| \frac{R_{bolo}^2}{(2\Delta\omega L)^2} \right| \tag{2.24}$$

For EBEX we had inductors of $L_{EBEX} = 24\ \mu H$ and frequency spacing of at least $\Delta\omega = 2\pi \cdot 60\ kHz$. For a detector dropped to 85% in the transition, a normal resistance of 1.5 Ω resulted in predicted electrical cross-talk at a level of 0.5%.

Transition Temperature

The TES was a bilayer of titanium atop aluminum. The titanium thickness was fixed at ∼110 nm. Depending on the wafer, the aluminum thickness varied from ∼30 to 50 nm. The critical temperature was controlled by the aluminum layer thickness, where the thinner aluminum layer provided a lower critical temperature (and also a higher normal resistance).

The ideal critical temperature minimized the phonon noise for detectors at the EBEX bath temperature. To express the phonon NEP as a function of our measurable quantities, we replaced gamma by equation 2.21 and let $G = dP/dT$. The phonon NEP as a function of the critical temperature T_c, the power of thermal conductivity n, the power to hold the detector in the transition P_{sat}, and the bath temperature T_{bath} is

$$NEP_{phonon}^2 = 4k_B T_{bath} P_{sat} \frac{(n+1)^2}{(2n+3)^2} \frac{\left(\frac{T_c}{T_{bath}}\right)^{2n+3} - 1}{\left(\left(\frac{T_c}{T_{bath}}\right)^{n+1} - 1\right)^2} \tag{2.25}$$

We assumed T_{bath} was 260 mK, P_{sat} was 6 pW, and n was in between one and three, Figure 2.4. For $n = 3$, the phonon NEP was minimized at a ratio of transition temperature to bath temperature, $\frac{T_c}{T_{bath}}$, of ∼1.7. The EBEX bath temperature was expected to be ∼260 mK and during the detector fabrication n was assumed to be 3. This put the target critical temperature for all EBEX observation frequency bands at 440 mK, Table 2.2.

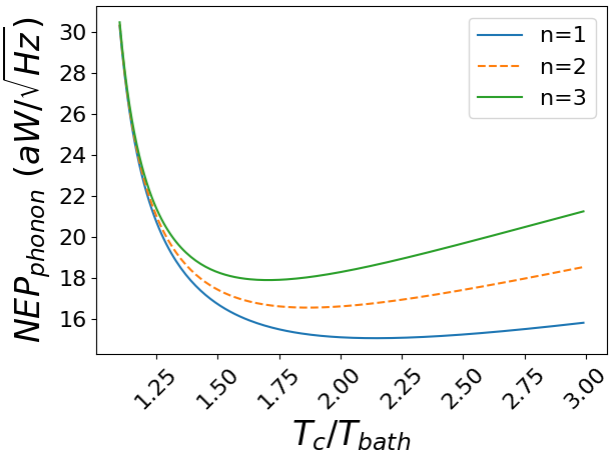

Figure 2.4: Phonon NEP as a function of the ratio of critical temperature to bath temperature for three different values of the thermal conductivity power. The goal was to choose T_c such that phonon noise was minimized.

Thermal Conductance

Ground-based telescopes design their detectors to accommodate the radiative load and fluctuations from the atmosphere. Long-duration balloon flights, however, typically float at an altitude of ∼120,000 ft, above ∼98% of the atmosphere. Without any adjustments to detector fabrication, the photon NEP in a space-like environment is improved relative to on the ground because of the decrease in radiative power absorbed, Equation 2.22. The decrease in radiative power also allows for, with adjustment to detector fabrication, a decrease in the phonon NEP. The smaller radiative load allows for a smaller dynamic range which allows for a smaller G, Equation 2.1. The goal was to minimize G, in order to minimize the phonon NEP, while keeping G large enough for the detectors to not saturate in the presence of the radiative load at float.

Table 2.1 summarizes the calculation of the target average thermal conductances. For EBEX at float, the predicted radiative loads on the detectors were 2.4, 7.3, and 12 pW for the 150, 250, and 410 GHz observation bands. Assuming bolometer absorption efficiencies of 0.6, 0.5, and 0.4 for the 150, 250, and 410 GHz bands, the predicted absorbed radiative powers were 1.4, 3.6, and 4.6 pW, respectively. The EBEX detectors

inherited their initial design from ground-based telescopes, Atacama Pathfinder Experiment (APEX) and the South Pole Telescope. At 150 GHz, the expected radiative load was a factor of roughly 10 less than the ∼15 pW load observed at 150 GHz by APEX [39]. In order to take advantage of the decrease in radiative load at float and increase the detector sensitivity, the fabrication goal was to lower the average thermal conductance for the 150 GHz detectors to 20 pW/K. In order to decrease G for the 150 GHz detectors, the spiderweb legs were roughly doubled in length, from 0.5 mm to 1.05 mm, and two of the legs were decreased in width from 17 μm to 6 μm, right panel of Figure 2.3. The average thermal conductance goal for the 250 GHz was 50 pW/K and for the 410 GHz detectors was 60 pW/K, Table 2.1. This design goal provided a safety factor of 2.5, for all observation frequency bands, in case of unanticipated radiative load or fluctuations.

Freq (GHz)	P_{input} (pW)	ϵ	$P_{absorbed}$ (pW)	× Safety Factor	Target $\overline{G}$
150	2.4	0.6	1.4	4	19
250	7.3	0.5	3.7	9	45
410	12	0.4	4.7	12	63

Table 2.1: For each observation frequency, the path to the target average thermal conductance. P_{input} was calculated given all of the predicted transmissions and reflections of all of the optical elements. ϵ is the detector absorption efficiency assumed. $P_{absorbed}$ is the predicted absorbed power, $P_{input} \cdot \epsilon$. All frequency bands were multiplied by a safety factor of 2.5. The target $\overline{G}$ was $P_{absorbed}/\Delta T$, where ΔT was the target T_{crit}=0.44 K minus the expected T_{ebex}=0.25 K.

Time Constant

The TES' intrinsic thermal time constant was $\tau_0 = C/G$ and it was sped up by electrothermal feedback to give $\tau_{ETF} = \tau_0/(1 + \mathscr{L})$. The time constant target was set by the bolometer's LCR filter bandwidth and by the telescope scan speed. Relative to the ground-based telescopes, the time constant needed to be held approximately constant because we used the same DfMUX electronics and because EBEX was to have roughly the same scan speed. Since the thermal conductance, G, was decreased relative to the ground-based detector design, in order to keep τ constant, the heat capacity, C, also

needed to be decreased. During the fabrication process for the APEX ground-based detectors, the bling in the center of the web was made of 500-700 nm of gold [39]. For the EBEX detectors, we decreased the total thickness of the gold deposited to 20 nm. This provided the dominant heat capacity for the detector and was expected to be 0.5 pJ/K for all observation frequency bands. The target time constants at zero loopgain were calculated by taking the ratio of the expected heat capacities to the target thermal conductances. We used Equation 3.8 and assumed a power of thermal conductivity of 2 to convert the target average thermal conductances to target dynamic thermal conductances. This gave target time constants of 17, 13, and 10 ms for the 150, 250, and 410 GHz bands, Table 2.2.

Band (GHz)	150		250		410	
	Design	Measured	Design	Measured	Design	Measured
R_n (Ω)	1.5	1.9	1.5	1.5	1.5	1.4
T_c (K)	0.44	0.45	0.44	0.48	0.44	0.47
$\overline{G}$ (pW/K)	19	39	45	53	63	63
τ_0 (ms)	17	88†	13	46†	10	57†

† Median of measurements on a single wafer at each frequency; see EBEX Paper Two [29].

Table 2.2: Designed and measured detector parameters for each of the frequency bands. The values in the 'Measured' columns are median values for all detectors on the wafers used for flight. Description of the measurements, histograms, and further discussion of the measured values are given in Chapter 3.

Chapter 3

Detector Characterization

There were more than four dozen detector wafers fabricated and characterized for EBEX. The wafer naming convention was *frequency band - position in fabrication sequence*, e.g. 250-04 was the fourth 250 GHz wafer to be fabricated. I performed the characterization measurements in testbeds designed to be as similar to the final flight configuration as possible. The three testbeds used were: a dedicated EBEX test cryostat (ETC) at the University of Minnesota, a test cryostat at McGill University, and the EBEX cryostat itself, made dark. In the characterization measurements I report here, I mounted the wafer and coupled it to the readout electronics as I did for flight, Section 1.3. The wafers were cooled to 250-320 mK, where the exact temperature depended on the testbed.

As the fabrication procedure was modified to build detectors optimized for a space-like environment, I measured the detector parameters in the dark cryostats to provide feedback to fabrication. The detector parameter measurements also enabled me to estimate the sensitivity the detectors would be able to achieve.

3.1 Detector Parameter Measurements

The main detector parameters I measured for each detector were normal resistance, critical temperature, and thermal conductance. For a subset of wafers, I also measured time constants, both electrothermal and optical. There was a dedicated cooldown in ETC to measure the optical efficiency of a subset of 150 GHz detectors.

3.1.1 Normal Resistance

In order to get the bolometer resonant frequencies and their normal resistances, I performed a network analysis on each comb with the bath held a couple hundred millikelvin above the critical temperatures. The network analysis swept a voltage across the comb in frequency and measured the current response of the circuit, Figure 3.1. At each bolometer's LC resonant frequency, the multiplexed LCR circuit peaked in current.

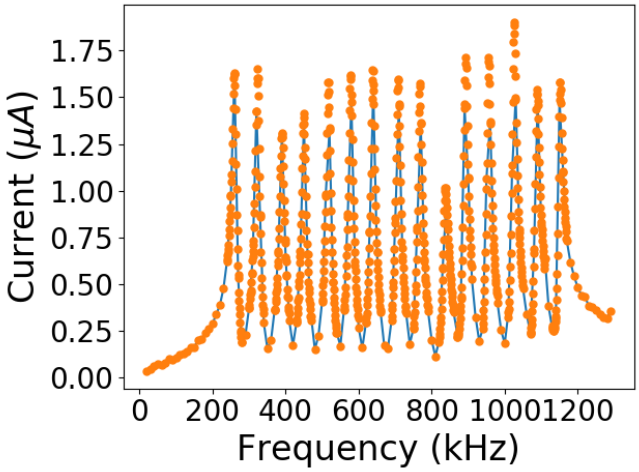

Figure 3.1: An 800 mK network analysis from wafer 150-17. The blue line has frequency steps of 10 kHz to roughly locate the peaks and the orange dots are finer scans with steps of 1 kHz to obtain the data to fit.

The impedance as a function of frequency, ν, for each bolometer in series with its inductor, $L = 24\ \mu H$, and capacitor, C_i, was modeled as

$$Z_{LCR_i}(\nu) = \sqrt{R_i^2 + \left(2\pi\nu L - \frac{1}{2\pi\nu C_i}\right)^2} \tag{3.1}$$

where R_i was the i^{th} bolometer's resistance. There was also a stray inductance, L_x, and stray capacitance, C_x, in parallel with the detector comb. The network analysis current for each peak was thus

$$I = \frac{V_{bias}}{|Z_{LCR_i} + j2\pi\nu L_x + \frac{1}{j2\pi\nu C_x}|} \tag{3.2}$$

Figure 3.2 shows a single peak and the fit to the model. Note, the frequency at the maximum current and the optimal bias frequency are not necessarily aligned because I

wanted to maximize the current through the bolometer rather than maximize the current through the entire circuit (which included the stray capacitance and inductance).

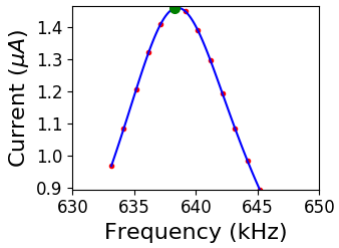

Figure 3.2: The Lorentzian fit (blue line) to a network analysis peak (red dots). The fit provides the bolometer resonant frequency (green dot), the bolometer normal resistance, and the circuit's stray inductance and stray capacitance.

Around 800 mK, when both the niobium leads on the wafer and the aluminum wire-bonds between the wafer and the LC board were superconducting, the fit provided the normal resistance of the TES. Histograms summarizing the measured normal resistance values for the flight wafers, broken down by frequency band, are shown in Fig. 3.3. The median normal resistance, R_{normal}, for the 150, 250, and 410 GHz bands was 1.9, 1.5, and 1.0 Ω respectively. The 150 and 410 GHz bimodal distributions were due to detector parameters being closely grouped within a single fabrication run, but varying between fabrication runs. The measured value of R_n for the 250 GHz band closely matched the design (see Table 2.2). For the other two frequency bands, one mode of the distribution closely matched while the other mode was higher (lower) than design for the 150 (410) GHz band. The 150 GHz detectors with a measured R_n of 1.9 Ω, instead of the nominal 1.5 Ω, I calculated to have increased electrical cross-talk from a value of 0.5% to 0.9% and decreased loopgain by 30%. The 410 GHz detectors with a measured R_n of 1 Ω, two-thirds of the design value, I calculated to have increased Johnson noise by 20% relative to the nominal expected value of 4.0 pA/$\sqrt{\text{Hz}}$ (9.4 aW/$\sqrt{\text{Hz}}$); see Equation 2.18.

3.1.2 Critical Temperature

For the measurement of the critical temperature in ETC, I placed a voltage bias of 5 nV_{rms} across the detector such that the Joule heating of $\frac{V^2}{R} = 1.5\ fW$ was negligible

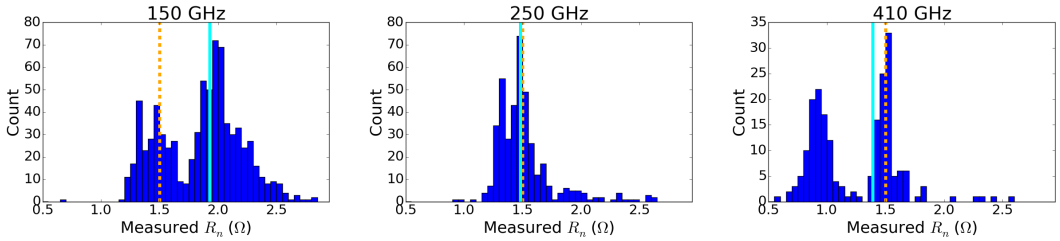

Figure 3.3: Histogram of measured normal resistances R_n for each of the frequency bands, including the median (vertical cyan) and design (vertical gold dashed) values.

but there was still a measurable current signal. I slowly, less than 3 mK/min, dialed the temperature up and down to move the bolometers through their superconducting transitions. Changing the temperature slowly was important because the temperature was read out from a sensor attached to the underside of the invar plate onto which the wafer was mounted and the bolometers were only weakly coupled to the bath via their spiderweb legs. I used the bath temperature as a proxy for the bolometer temperature. Without time to thermalize, there would have been significant hysteresis. This measurement also relied on the cryostat being dark because radiative power would have increased the temperature of the detector but not the bath where the temperature sensor was mounted. Fig. 3.4 is an example of a critical temperature measurement for a bolometer on wafer 150-02. I measured demodulated analog-to-digital converter (ADC) counts with the DfMUX boards and converted to resistance using the measured current and voltage transfer functions and Ohm's law, $R = V_{bias}/I_{measured}$. When the TES was superconducting, there was an offset in the resistance measured because there was still current due to the non-zero stray impedance.

Histograms summarizing the measured critical temperatures for the three EBEX frequency bands are shown in Fig. 3.5. The median critical temperatures, 0.45, 0.49, and 0.51 K for the 150, 250, and 410 GHz bands, respectively, were within 16% of the target value of 0.44 K. The greatest spread in measured values of T_c was in the 150 GHz band. The effect of this spread is to increase Johnson (phonon) noise when T_c is above (below) the design value. At the high (low) edge of the distribution with $T_c = 0.54$ K (0.36 K), there was an 11% (5%) increase in the calculated Johnson (phonon) noise relative to the nominal expected value of 4.0 pA/$\sqrt{\text{Hz}}$ (20 aW/$\sqrt{\text{Hz}}$).

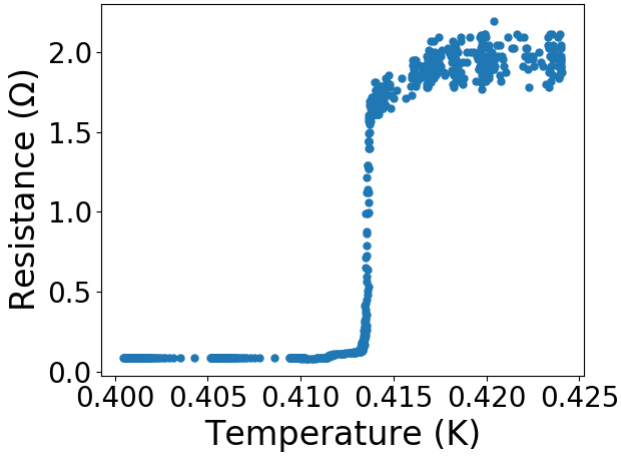

Figure 3.4: Resistance as a function of bolometer temperature for a detector from wafer 150-02. The resistance was the ratio of the voltage bias across the bolometer to the current measured through the SQUID. This bolometer had a T_c of ∼414 mK.

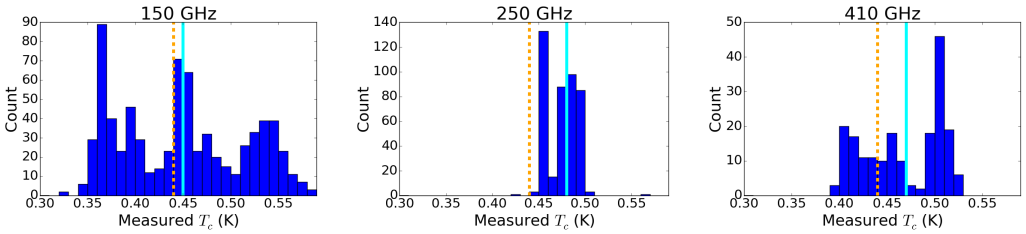

Figure 3.5: Histogram of measured critical temperature values for the detectors in each frequency band including the median (vertical cyan) and design (vertical gold dashed) values.

3.1.3 Thermal Conductance

The dark test cryostat measurements of the thermal conductance of the link from the TES to the bath allowed me to predict the phonon NEP for each detector and also determine if there would be sufficient dynamic range to operate the detectors under the expected loading conditions. I wanted to minimize G so that the detector NEP was minimized and thus the detector sensitivity was maximized. The value of G, however, needed to be sufficiently high to allow for the detectors to operate in the presence of the radiative load at float, Section 2.2.

In order to measure the thermal conductance of the link, I stepped down the voltage bias, typically in steps of 0.05 μV, and measured the current through the TES. At each step, I calculated the instantaneous resistance, the ratio of the voltage bias to the current measured, Figure 3.6. I dropped the bias voltage of each bolometer until the ratio of the voltage bias to the current measured reached a fixed fraction of its original value. In the test cryostats, the fraction was typically 0.7. For EBEX2013 (EBEX2013), the fraction was 0.85 for the majority of flight. The value used in flight was higher than the nominal lab value because in the test cryostats the bolometer noise performance deeper in the transition diverged from the predictions, Section 3.2.

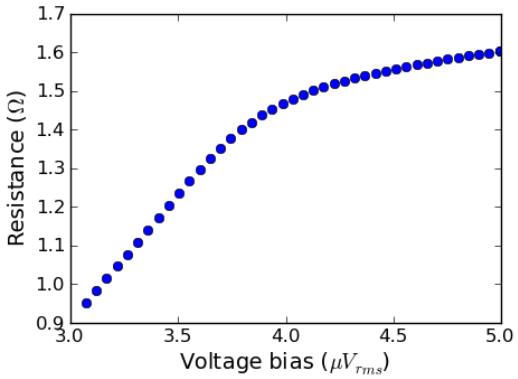

Figure 3.6: The instantaneous resistance ($\frac{I}{V}$) of a 150-01 bolometer as a function of the voltage bias across the bolometer. This bolometer was dropped to 0.6 of the starting value.

The left panel of Figure 3.7 is an IV curve, the current measured as a function of

the voltage bias across the TES, for one detector on wafer 150-01. Above the superconducting transition, at higher voltage biases, the AlTi bilayer of the TES was normal and so the current was proportional to $1/R$. Fitting the linear, normal region for this particular detector gave a resistance of 2.2 Ω. As the bilayer began to superconduct, the resistance dropped and the current measured turned around. Once the bolometer was sufficiently far into the superconducting transition, negative electro-thermal feedback kept the power dissipated in the bolometer at a fixed level, Section 2.1. The right panel of Figure 3.7 is a PV curve, the power dissipated in the bolometer ($I \times V$) as a function of the voltage bias. The electrical power required to hold the detector in the transition is the horizontal section of the PV curve, ∼10 pW for this detector.

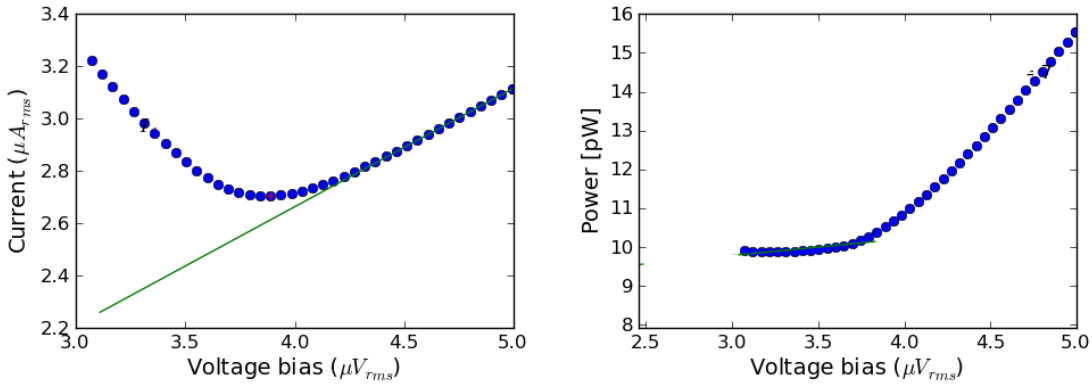

Figure 3.7: Left: The current through the SQUID as function of the voltage bias across the bolometer. Right: The electrical power dissipated in the bolometer ($I \times V$) as a function of the voltage bias across the bolometer.

For the dark characterization tests, because each bolometer wafer was enclosed in a light-tight box which was heat sunk to the bath, the radiative power on the bolometer should have been negligible. In the case of a negligible radiative load, the total electrical power measured from the PV curve was the total power dissipated in the detector. This power was often referred to as the saturation power, P_{sat}. The saturation power was a useful parameter to think in terms of because the bolometer lost nearly all sensitivity if it saturated, i.e. if P_{sat} was less than or near to the radiative load during observations.

I calculated the average thermal conductance of the weak link for each detector from

P_{sat}, measured from the PV curve, and its measured critical temperature, Section 3.1.2,

$$\overline{G}(T_{bath}) = \frac{P_{sat}(T_{bath})}{T_c - T_{bath}} \tag{3.3}$$

$\overline{G}$ is a function of the bath temperature. The test cryostats operated at different bath temperatures than EBEX, so the measured $\overline{G}$s needed to be adjusted to the EBEX bath temperature. If the phonon transport along the weak link was diffusive, as opposed to ballistic (where the mean free path of the phonon was much longer than the length of the material in the direction of travel), then the thermal conductivity followed a power law,

$$\kappa\left(T\right) = \kappa_0 T^n \tag{3.4}$$

where n was the power of the thermal conductivity. Normal metals have $n = 1$ while crystalline dielectrics or superconductors have $n = 3$ [36]. The 2009 EBEX test flight wafers were measured to have n values of 2.2 ± 0.3, 1.9 ± 0.2, and 2.1 ± 0.2 for the 150, 250, and 410 GHz bands respectively [43]. If the weak link had a uniform cross section of area A and length l, then the thermal conductance was

$$G = \frac{A}{l}\kappa_0 T^n \tag{3.5}$$

and the power flow was described by

$$P = \int \frac{dP}{dT}dT = \int_{T_{bath}}^{T_c} \frac{A}{l}\kappa_0 T^n dT = \frac{A\kappa_0}{l(n+1)}\left(T_c^{n+1} - T_{bath}^{n+1}\right) \tag{3.6}$$

Letting this equal equation 2.1 and then taking the ratio of the power in EBEX to the power in the test cryostat, I found the corrected thermal conductance at the EBEX bath temperature, T_{ebex}, to be

$$\overline{G}\left(T_{ebex}\right) = P_{sat,test}\left(T_c - T_{ebex}\right)\frac{\left(T_c^{n+1} - T_{ebex}^{n+1}\right)}{\left(T_c^{n+1} - T_{test}^{n+1}\right)} \tag{3.7}$$

where $P_{sat,etc}$ was the saturation power measured in the test cryostat, T_c was the measured critical temperature, and n was the power of the thermal conductivity from the EBEX test flight wafer measurements. For NEP predictions, I assumed the same power law form of the thermal conductivity and related my measurement of $\overline{G}$ to G via Lee [35]

$$G = (n+1)\frac{1 - \frac{T_{bath}}{T}}{1 - \left(\frac{T_{bath}}{T}\right)^{n+1}}\overline{G} \tag{3.8}$$

Histograms summarizing the measured average thermal conductance values, corrected to an EBEX bath temperature of 0.25 K, for the three observation frequency bands are shown in Figure 3.8. I found the median average thermal conductance, $\overline{G}$, for the 150, 250, and 410 GHz bands to be 36, 51, and 69 pW/K respectively. The target values for the average thermal conductances were set by the radiative loading in the balloon environment, Section 2.2, and were 19, 45, and 63 pW/K for the 150, 250, and 410 GHz bands respectively. The goal was to err on the higher side of the target and take the moderate hit in phonon noise rather than risk rendering the detectors inoperable because of too little thermal conductance for the radiative load. While the measured medians are up to 40% larger than the design values, the spread in the measurements is even larger. This spread is a consequence of variance between wafers and is also apparent in the measurements of T_c. A thermal conductance 40% higher than the target, for a median 410 GHz detector, increased the phonon NEP by 12% relative to the nominal value of 26 $aW/\sqrt{Hz}$.

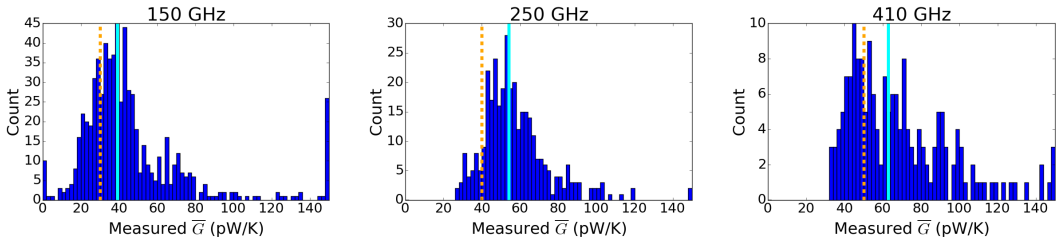

Figure 3.8: Histograms of the measured average thermal conductance values for the three frequency bands including the median (vertical cyan) and design (vertical gold dashed) values. The measurements of $\overline{G}$ exceeding 150 pW/K are piled into the last histogram bin.

3.1.4 Optical Efficiency

In order to measure the optical efficiency of the EBEX bolometers, the bolometers needed to observe a known, controllable radiative load. This radiative load was provided via a blackbody, a body absorbing all incident radiation falling upon it. My ETC blackbody was inspired by the design of Peterson and Richards for calibrating IR photometers [44]. The blackbody itself was an inverted cone with an angle of 37°,

Figure 3.9. I made the blackbody by pouring castable Eccosorb CR-110 into a teflon mould and baking it. For mm-wave radiation incident on flat Eccosorb CR-110 at cryogenic temperatures, 30% is reflected and 70% refracted [44]. The refracted radiation was absorbed inside the cone. The reflected radiation for the light ray with the outermost angle, the one with the fewest number of bounces, reflected off the Eccosorb surface four times. Fewer than 8 parts in 1000 of the incident radiation escaped the blackbody. A steeper cone would have had greater absorptivity, but the height was limited by the dimensions of the ETC.

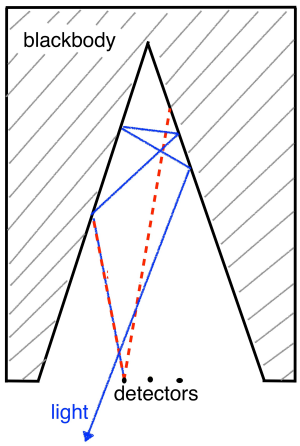

Figure 3.9: Eccosorb blackbody design above detectors (black dots). The detector's field of view (red dashed lines) was 20°. The blackbody cone had an opening angle of 37°. The outermost light ray (blue line) bounced off the surface of the blackbody four times.

The model of my optical efficiency testbed is shown in Figure 3.10. The wafer box was supported by a thin column of vespel mounted directly to the 4 K cold plate. For the hexagon of seven detectors open to the blackbody, the wafer box had a miniature gold-plated optics stack of wave guides and horns, to provide the high pass cutoff, and Cardiff LPE filter scraps, for the low pass cutoff. The blackbody was supported by a thin column of GR-10, also mounted directly to the 4 K cold plate. There was a cooper bar embedded inside the Eccosorb for mounting a temperature sensor. To cool the blackbody down from room temperature, another copper bar embedded in the

Eccosorb was connected to the 4 K plate via a gas-gap heat switch (not shown in the figure). For the optical efficiency measurements, the heat switch was opened and the blackbody temperature was controlled by a flat copper heater glued to the outside of the cone.

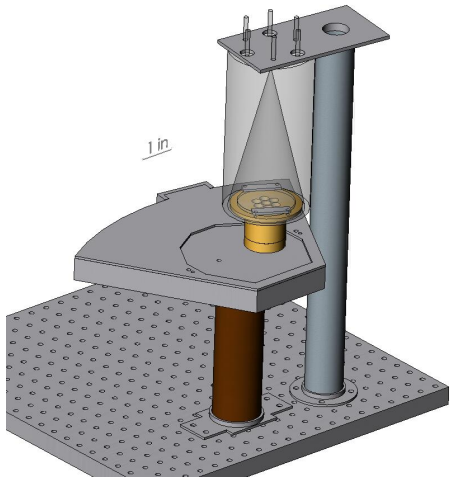

Figure 3.10: The model of the optical efficiency testbed in ETC. The blackbody is the partially transparent cone hanging from the metal plate attached to the top of the green GR-10 column. The grey wedge-shaped box atop the brown vespel leg encloses the wafer. There is a gold-plated stack of horns and waveguides, as well as a set of low pass filters, above a hexagon of seven detectors open to the blackbody. The wafer box and blackbody are both mounted to the 4.2 K cold plate.

The x8 multiplexing readout schematic for wafer 150-01 with the blackbody setup is shown in Figure 3.11. Each detector was represented by a circle with several identifying labels (the bolometer's row-column name, the wire bonding pad number, the channel number on the LC board, and the pin from the LC board to the SQUID board). There was a hexagon of 7 bolometers (outlined in pink), with an optical stack of wave guides, cones, and miniature EBEX low-pass radiative filters, open to the blackbody. The other detectors were looking at the 320 mK box enclosing them. The lines leading from each circle to the edge of the wafer were the bolometer's niobium leads to the wire bonding pads. The grouping of the bolometers read out by each SQUID were indicated by outlines of different colors. The non-functioning detectors were crossed off.

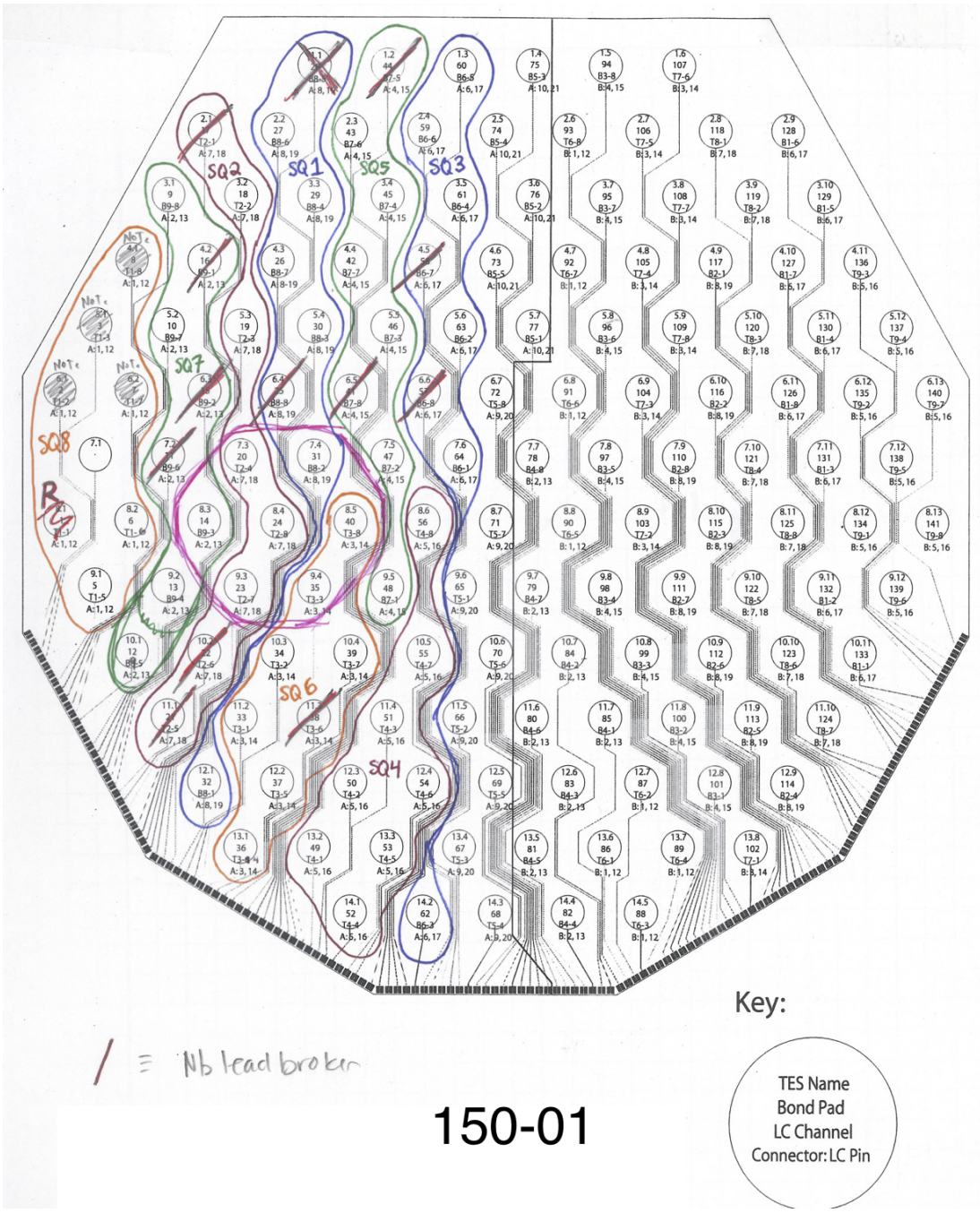

Figure 3.11: Blackbody setup x8 multiplexing readout setup for wafer 150-01. Within the pink ring were the hexagon of detectors open to the blackbody. Squid groups were outlined in different colors and labelled SQN, for $N \in (1, 8)$. Non-functioning detectors were crossed out.

The total power dissipated in the detector was

$$P = P_{elec} + \epsilon P_{rad} = \overline{G}\Delta T \tag{3.9}$$

where ϵ was the detector optical efficiency. For several blackbody temperatures, the electrical power required to hold the detector in the transition was measured, Figure 3.12. As the blackbody temperature increased, the electrical power decreased. By 9 K, the power from the blackbody alone saturated the detectors. That is, there was no turnaround observed in the IV curve, the bolometer was normal even when the electrical power was at zero.

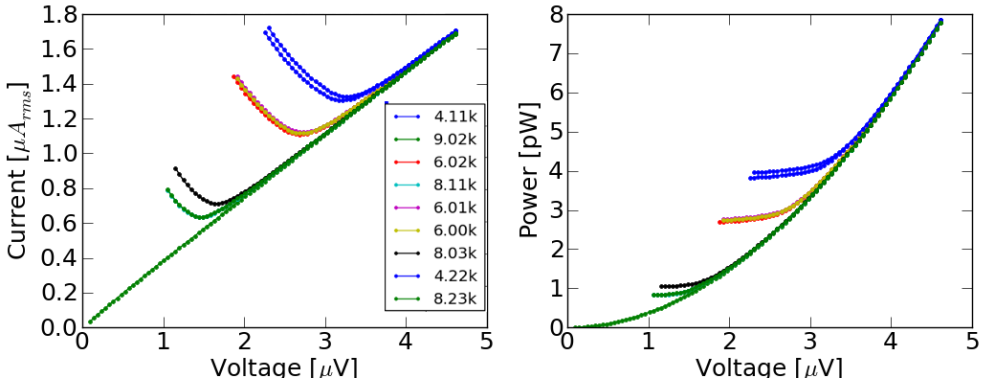

Figure 3.12: IV (left) and PV (right) curves for wafer 150-01 bolometer 8-04. The electrical power required to hold the detector in the transition decreased as the blackbody temperature increased.

I integrated the blackbody radiation curve over the EBEX 150 GHz observation band to determine the amount of power incident upon the detectors at each blackbody temperature, left panel of Figure 3.13. Rearranging Equation 3.9, I get the electrical power as a function of the radiative load

$$P_{elec} = \overline{G}\Delta T - \epsilon P_{rad} \tag{3.10}$$

The slope of the line is the optical efficiency, ϵ. The right panel of Figure 3.13 is the fit for wafer 150-01 bolometer 8-04. Table 3.1 gives the slope for each of the functioning bolometers open to the blackbody.

The detectors not open to the blackbody also saw a change in their electrical power as a function of the blackbody temperature. The IV and PV curves for a detector two rows

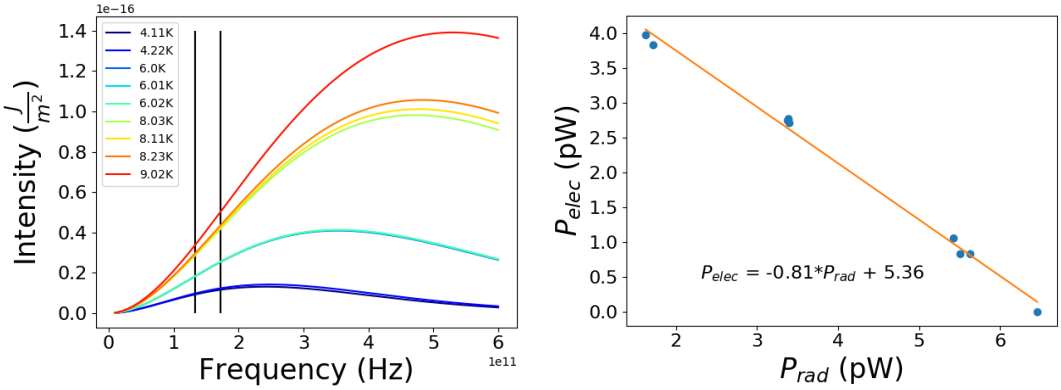

Figure 3.13: Left: Blackbody radiation as a function of temperature. The EBEX 150 GHz band is marked by the black vertical lines. Right: Wafer 150-01 bolometer 8-04 electrical power as function of blackbody power. The slope, ~ 0.8, is the detector's optical efficiency.

bolometer	efficiency
7-03	66%
7-04	87%
8-03	74%
8-04	81%
9-03	74%

Table 3.1: Measured optical efficiencies of wafer 150-01 bolometers open to blackbody in ETC. The average measured ϵ was 76% with a standard deviation of 8%.

away from the detectors open to the blackbody are shown in the left and middle panel of Figure 3.14. The electrical power as function of the blackbody power is shown in the right panel of Figure 3.14. This detector had a measured optical efficiency of 9%. The average optical efficiency and standard deviation for the seven dark detectors measured was $\epsilon = 10 \pm 1\%$. The optical cross-talk from radiation leakage in the integration cavity was expected to be less than 1% [42]. The excess can not be explained by a change in bath temperature because the bath increased by only 2 mK between a blackbody temperature of 4.2 K and 9 K. The excess is indicative of radiation from the blackbody entering the wafer enclosure via a route other than through the optics stack.

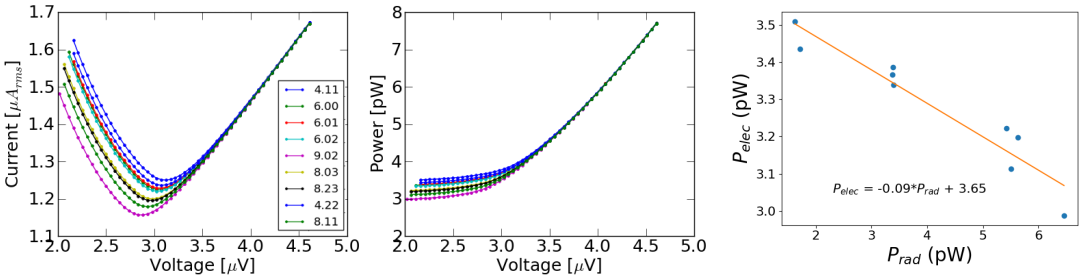

Figure 3.14: Left: Wafer 150-01 bolometer 10-01 IV curves as a function of blackbody temperature. Center: The PV curves for this same bolometer and same set of blackbody temperatures. Right: Though this detector was two rows away from the detectors open to the blackbody, the electrical power to hold the bolometer in its transition as a function of the black body power has a non-zero slope of -0.09.

3.1.5 Time Constants

Mounted to the lid of the dark wafer enclosure in ETC, directly above the detectors, I had three Fairchild IR LED56's, with a center wavelength of 940 nm. After dropping the detectors into their transitions, I pulsed the LED on and off with a square wave and measured the detector response. The normalized response, as a function of the square wave frequency, for a comb of detectors on wafer 150-02 is shown in Figure 3.15. I assumed the response had a single pole roll off and took the time constant was taken to be the -3dB point, Table 3.2. There is a more thorough measurement and analysis of optical time constants as a function of observation frequency band reported in Table 2.2

and discussed in [29].

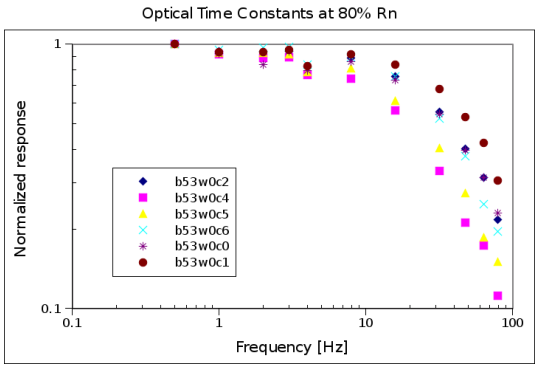

Figure 3.15: IR LED optical time constant measurement for a comb of six bolometers on wafer 150-02.

channel	frequency (Hz)	time constant (ms)
c0	18	8.8
c1	30.5	5.2
c2	20	8.0
c4	10	15.9
c5	10.5	15.2
c6	19	8.4

Table 3.2: IR LED time constants for one comb of bolometers on wafer 150-02. The bolometers were dropped to 80% of their initial resistance.

3.2 Dark Noise Performance

In order to understand the noise performance of each part of the detector readout chain, I broke down the noise measurements into room temperature electronics noise, electronics noise up to and including the 4 K SQUIDs, the noise of the bolometers normal with the stage above the bolometers' T_c, the noise of the bolometers held normal with the stage at the refrigerator's base temperature, and the noise of the bolometers in-transition as a function of their transition depth. The dark ETC had the exact same electronics boards, filters, and cables as EBEX.

3.2.1 Procedure

For each noise measurement, I took ∼3 minutes of data. I measured demodulated ADC counts with the DfMUX board and converted to physical units, typically nV, pA, or aW. The upper panel of Figure 3.16 is an example of a raw bolometer timestream converted to current for wafer 150-01 bolometer 3-01 as a function of sample number (there were 20 MHz/2^{17} = 190.73 samples per second). From the timestream, a gradient and offset were subtracted, a Hann window was applied, and the PSD was calculated. For the dark measurements, I report the noise level as the square root of the average of the PSD from 0.5 to 5.0 Hz. The lower panel of Figure 3.16 is the square root of the PSD with the red line indicating the average noise level.

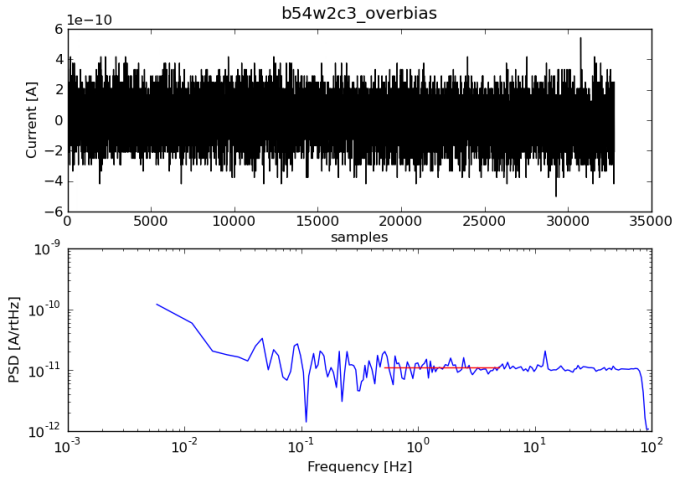

Figure 3.16: The raw bolometer timestream converted from ADC counts to current and the square root of the PSD for wafer 150-01 bolometer 3-01. The timestream was ∼3 minutes long. The white noise level was determined by averaging the PSD from 0.5 to 5 Hz and taking the square root. This bolometer had a white noise level of 11 $pA/\sqrt{Hz}$.

3.2.2 Test Cryostat Warm Electronics

With the SQUIDs off, I measured the open loop noise. This was a measure of the noise of the warm electronics referred back to the input of the SQUID controller first stage amplifier. The theoretical open loop transfer function was 0.774 nV to 1 ADC count.

The measured transfer function was a factor of 1.13 greater than the theoretical. Figure 3.17 is the measured open loop warm electronics noise, for two combs in ETC during the wafer 150-01 run, as a function of the demodulation frequency. The total noise prediction for the warm electronics components was 1.33 $nV/\sqrt{Hz}$, determined from the electronic specifications [45]. The largest contributors were the first stage amplifier of the SQUID controller board, Texas Instruments Op Amp 847 with a noise specification of 0.85 $nV/\sqrt{Hz}$, and that amplifier's 20 Ω gain defining resistor Johnson noise, 0.57 $nV/\sqrt{Hz}$. The measurement agreed with the prediction at low frequencies and then the signal rolled off, with a -3dB point around 1 MHz, because the first stage amplifier was being operated in the open-loop regime.

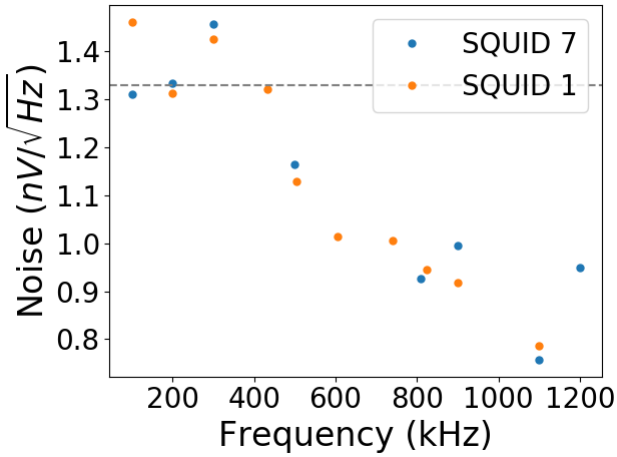

Figure 3.17: Measured noise of the warm electronics in ETC up to the first stage amplifier on the SQUID controller board. The open loop noise at low frequencies was predicted to be 1.33 $nV/\sqrt{Hz}$ and to roll off with a -3dB point around 1 MHz.

3.2.3 Test Cryostat SQUIDs

With the detectors at a temperature of 4.2 K, and without providing carrier or nuller biases, I measured the noise as a function of demodulation frequency. Away from the bolometer resonant frequencies, this is a measure of the noise due to the warm electronics and the SQUIDs.

With the SQUIDs tuned and their feedback loops closed, the warm electronic components' noise predictions were referred to current noise at the SQUID input coil. The SQUID transimpedance, dV/dI, was used to reference the noise of the SQUID controller first stage amplifier and its gain defining 20 Ω resistor. I measured dV/dI from the slope of the linear regime of the $V - \phi$ curve where we biased the SQUID, Figure 3.18. The fit to the line in the region where this particular SQUID from ETC was biased gives a transimpedance of $dV/dI = 375\ \Omega$. Note, the SQUIDs in EBEX were heat sunk to a colder temperature stage and so had a higher transimpedance on the order of 500 Ω. The SQUID flux-locked loop gain transfer function, $|\frac{(1-\mathscr{L}_{FLL})}{\mathscr{L}_{FLL}}|/R_{feedback}$ was used to reference the noise for those electronic components after the first stage amplifier. The amplifier's feedback resistor value was known, 5 $k\Omega$ for EBEX and 10 $k\Omega$ for ETC, and the flux-locked loop gain, $\mathscr{L}_{FLL}$, was estimated to be 13 [43].

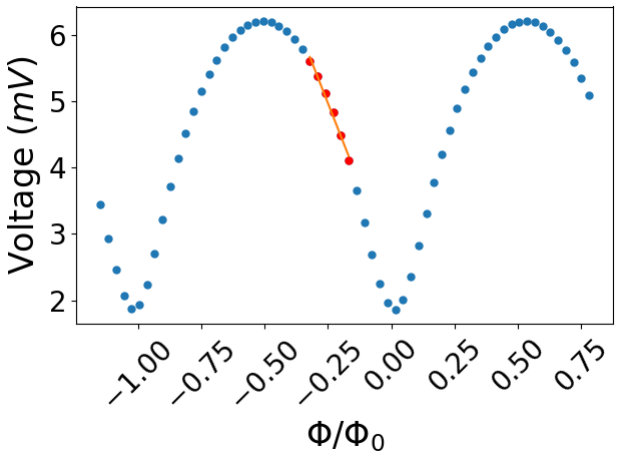

Figure 3.18: SQUID voltage versus flux curve. The operating regime is highlighted (red) and fit to a line (orange) to get the SQUID transimpedance.

Measurements of the electronics noise up to and including the SQUID are shown in Figure 3.19. These data are from the same two combs shown for the warm electronics noise. Earlier generations of this SQUID design were reported to have a noise of 2.5 $pA/\sqrt{Hz}$ [46]. Since the warm electronic noise agreed with predictions, Figure 3.17, the excess noise measured in ETC was assumed to be due to the SQUID. The blue line assumed an intrinsic SQUID noise of 2.5 $pA/\sqrt{Hz}$, while the orange line assumed

3.5 $pA/\sqrt{Hz}$. From here on out, I took the intrinsic SQUID noise to be 3.5 $pA/\sqrt{Hz}$.

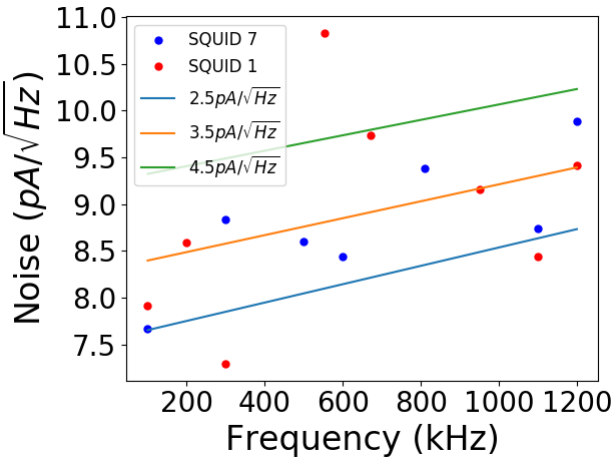

Figure 3.19: The measured electronic and SQUID noise (red and blue dots) as a function of demodulation frequency. The blue line is the noise prediction assuming the intrinsic SQUID noise is 2.5 $pA/\sqrt{Hz}$ while the orange line is assuming 3.5 $pA/\sqrt{Hz}$ and the green line is assuming 4.5 $pA/\sqrt{Hz}$.

3.2.4 Test Cryostat Johnson Noise

Figure 3.20 is the 4.2 K measured and predicted noise both on and off bolometer resonant frequencies. This data is from the same two combs, SQUIDs 1 and 7, on wafer 150-01 for which the warm electronics noise was measured. Demodulating away from the bolometer resonant frequencies gave just the electronic and SQUID noise discussed in Section 3.2.3. Demodulating at the bolometer resonant frequencies gave a measure of the 4.2 K bolometer Johnson noise in addition to the electronic and SQUID noise. The 4.2 K Johnson noise, for a bolometer at its normal resistance of 2 Ω was $\sim$ 11 $pA/\sqrt{Hz}$. These particular combs showed unexplained, abnormally high Johnson noise at demodulation frequencies around 800 kHz. Those bolometers would have had to have a resistance of 1.3 Ω at 4.2 K in order to give a total noise level of 16 $pA/\sqrt{Hz}$. It is unlikely I overestimated the resistances because I assumed the bolometer normal resistances from the $\sim$800 mK network analysis and the bolometer resistance actually increased, albeit with a shallow slope when normal, as the temperature increased.

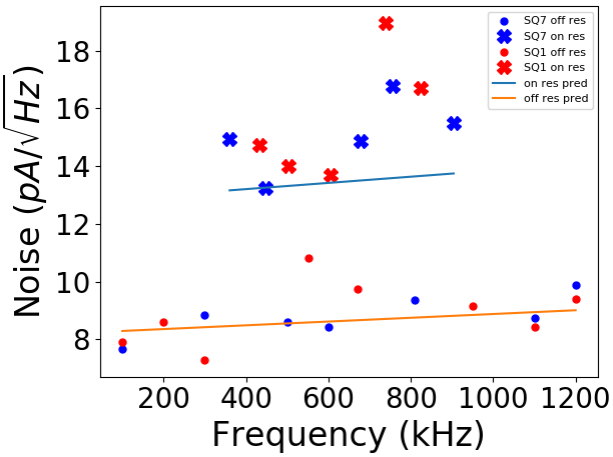

Figure 3.20: Electronic, SQUID, and Johnson noise in ETC as a function of demodulation frequency at 4.2 K. Off-resonance (dots, orange line) is just electronic and SQUID noise, while on-resonance (x's, blue line) includes the 4.2 K bolometer Johnson noise. There are neither carriers nor nullers on for these measurements.

Figure 3.21 is the 770 mK measured and predicted noise both on and off bolometer resonant frequencies, still with no carrier or nuller biases. This data is from a single comb, SQUID7, on wafer 150-01. The off-resonance noise included the electronic and SQUID noise while the on-resonance noise also included the 770 mK bolometer Johnson noise, $\sim 5pA/\sqrt{Hz}$ for a 2 Ω bolometer. The two lowest frequency off-resonance noise measurements were near the prediction. At the higher off-resonance demodulation frequencies, however, the measured noise was at the level of the on-resonance prediction, ∼15% above the off-resonance prediction. Though I expected the electrical cross-talk to increase to more than 1% given the larger detector resistance in this configuration, that was not enough to explain the level of excess noise we measured off-resonance. The on-resonance noise measurements at 770 mK agree more closely with the prediction than they did at 4.2 K. The improved agreement at the lower temperature was not understood.

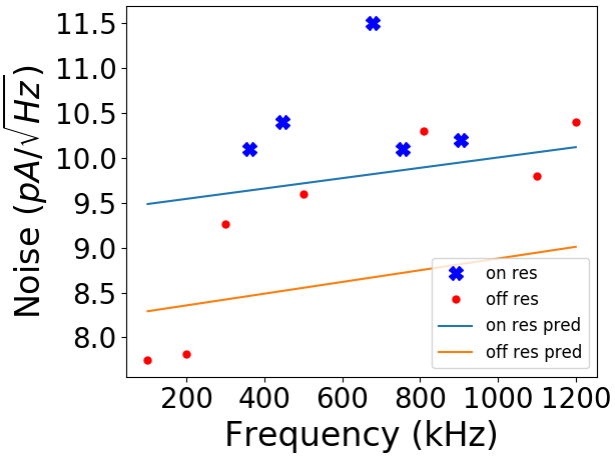

Figure 3.21: Electronic, SQUID, and Johnson noise in ETC as a function of demodulation frequency at 770 mK. Off-resonance (red dots, orange line) is just electronic and SQUID noise, while on-resonance (blue x's, blue line) includes the 770 mK bolometer Johnson noise. There are neither carriers nor nullers on for these measurements.

3.2.5 Test Cryostat Bolometer Overbiased Noise

When the detector was held above its transition, either via a warm bath or via an electrical bias, it was said to be overbiased. The overbiased noise included the electronic, SQUID, and bolometer Johnson noise. The contribution from the electronics was higher than when I measured the Johnson noise in Section 3.2.4 because there were carriers and nullers provided in order to electrically overbias the detectors. Near a bias frequency of 600 kHz, without carriers and nullers on, the electronics noise was $\sim 8.5\ pA/\sqrt{Hz}$. Also, the bolometer Johnson noise was higher because when overbiased, the bolometer temperature was higher. From Equation 2.1, I estimated the overbiased bolometer temperature to be

$$T_{bolo} = T_{bath} + \Delta P * \overline{G} \tag{3.11}$$

where ΔP is obtained from the PV curve, $\Delta P = P_{overbias} - P_{transition}$. Figure 3.22 is the measured and predicted overbiased noise for the SQUID7 comb of detectors on wafer 150-01 at a bath temperature of 340 mK. The measured overbiased noise agreed with the prediction.

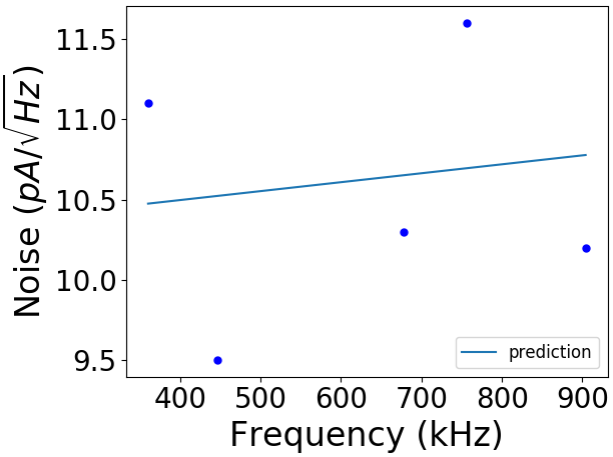

Figure 3.22: Overbias noise (blue dots) for one comb of detectors in ETC as a function of demodulation frequency at 340 mK. The prediction (blue line) includes electronic, SQUID, and overbiased bolometer Johnson noise. There are both carriers and nullers on for this measurement.

3.2.6 Test Cryostat In-transition Noise

The dark in-transition noise prediction included the electronic, SQUID, bolometer Johnson, and phonon noise. The left and right panels of Figure 3.23 are the measured and predicted in-transition noise for two different bolometers on wafer 150-01. In order to ensure the system was as clean as possible, only SQUID7 was tuned. There were five bolometers on the comb and four were overbiased while the in-transition noise measurements on the fifth bolometer were performed. Between each measurement, I re-overbiased the bolometer so it was always dropped relative to the same initial resistance. The dark noise measurements were referred to current through the SQUID. The phonon NEP prediction, a power noise, was multiplied by the current responsivity, dI/dP, to convert from power to current,

$$N^I_{phonon} = \sqrt{\gamma 4 k_B T^2 G}\left(\frac{\sqrt{2}}{V_{bias}}\right)\left(\frac{\mathscr{L}}{\mathscr{L}+1}\right) \tag{3.12}$$

If the bolometer was deep in the transition, then the loopgain, $\mathscr{L}$, was high and the responsivity was just a function of the voltage bias, $S_I = \frac{\sqrt{2}}{V_{bias}}\frac{\mathscr{L}}{\mathscr{L}+1} \approx \frac{\sqrt{2}}{V_{bias}}$. The loopgain was difficult to properly estimate, so the phonon noise prediction in the plot assumed

the bolometer was deep in the transition once we had dropped it any amount. That is, overbiased, at a fraction of $R_{initial} = 1$, I did not include the phonon noise in the prediction, but for all of the other fractions of $R_{initial}$, I assumed the bolometer was in the high loopgain regime. Towards the top of the transition, at higher fractions of $R_{initial}$, the bolometer was not deep in the transition and $\mathscr{L}$ was not large. In this case, the phonon noise contribution to the prediction was overestimated. If $\mathscr{L} = 1$, as was the case at the turnaround of the IV curve near $R = 0.98 \times R_{initial}$, by making this assumption, I overestimated the phonon contribution by a factor of 2, which decreased the total noise prediction from 13 $pA/\sqrt{Hz}$ to 12 $pA/\sqrt{Hz}$.

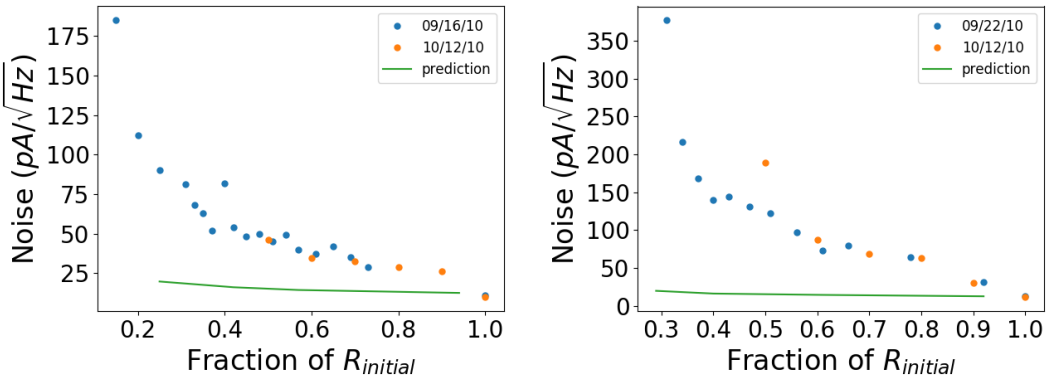

Figure 3.23: In-transition noise in ETC for wafer 150-01 bolometer 3-01 (left) and bolometer 5-02 (right). The prediction (green line) includes electronic, SQUID, Johnson, and phonon noise. The measurements were repeatable across multiple days (blue vs orange dots). The overbiased noise, at $R_{initial}$, agreed with predictions, but as the depth in transition increased, the discrepancy between the prediction and measurement increased. The noise performance was repeatable across different days, which meant different fridge cycles and different detector tunings.

The data (blue and orange dots) lay atop the prediction (green dot) at $1.0 \times R_{initial}$, i.e. overbiased. This agreement is consistent with the overbiased noise measurements and predictions performed on the entire comb. Already by the time the detector was at $0.9 \times R_{initial}$, the measured noise was a factor of two greater than the prediction. The discrepancy between the measured and predicted noise increased as I dropped the detector to lower fractions of $R_{initial}$. The detector wasn't latched because I was able

to successfully re-overbias between each measurement. There could have been an unfiltered, unaccounted for radiative load during the wafer 150-01 cryostat run because it was performed with the optical efficiency setup in which there was a hexagon of seven detectors open to the blackbody. The detectors shown in Figure 3.23 were two (bolometer 5-02) and four (bolometer 3-01) bolometers away from detectors open to light, see Figure 3.11. Assuming the loopgain at 0.9 $\times R_{initial}$ is high enough to approximate the current responsivity as $\sqrt{2}/V_{bias}$, then bolometer 3-01 would have had to absorb 11 pW of radiation in order to bring its prediction in line with its measurement. Bolometer 5-02 would have had to absorb 17 pW. For comparison purposes, the in-band 4.2 K blackbody emission was predicted to be 1.7 pW.

The excess noise in-transition was observed on several wafers. Figure 3.24 shows a measurement performed as described above, except it was for a bolometer on wafer 150-02 and the wafer was enclosed in the nominal ETC dark box instead of housed in the optical efficiency setup. As with wafer 150-01, the overbiased noise agreed with the prediction. The measurement at 0.9 $\times$ $R_{initial}$ was within 5% of the prediction, which included SQUID, electronic, Johnson, and phonon noise (assuming large $\mathscr{L}$). At 0.8 $\times$ $R_{initial}$, however, the measurement exceeded the prediction by 40%. I suspect as I dropped the bolometer deeper into the transition, the bolometer response was in the unstable regime and experienced exponentially growing oscillations. For the detectors at float, I chose, in part, to drop them to a fraction of 0.85 $\times R_{initial}$ because this was the boundary at which the noise performance deteriorated.

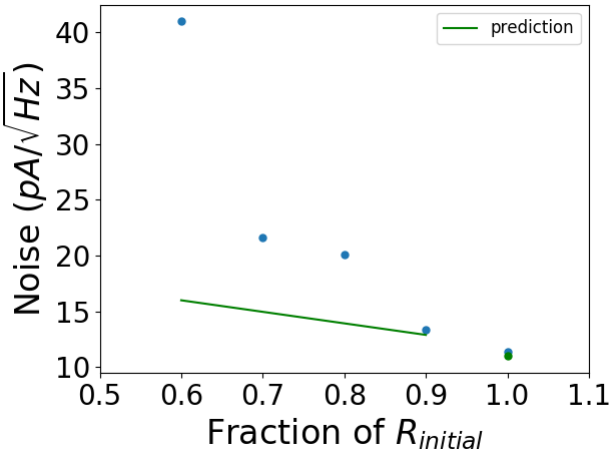

Figure 3.24: 150-02 in-transition noise for bolometer 2-08. The prediction for the overbiased noise, at a fraction of $R_{initial} = 1$, is a green dot and the measurement a blue dot. The overbiased noise prediction includes electronic, SQUID, and Johnson noise, but not phonon. The in-transition noise prediction, which includes phonon noise, is the green line and the measurements are the blue dots.

Chapter 4

Detector In-Flight Performance

I discuss the detector yield, Section 4.1, and the detectors' measured radiative loads, Section 4.2. In section 4.3, using the dark characterization measurements, the measured radiative load, the electrical bias parameters, and the DfMUX transfer functions, I predict the instrument sensitivity in NEP. I report on the noise performance of each detector by comparing its expected NEP to the median of its measured NEP over all portions of the EBEX flight for which it had valid data.

4.1 Detector Yield

	150 GHz	250 GHz	410 GHz	Total
Total number of bolometers on wafers	1120	560	280	1960
Able to read out with EBEX electronics	992	496	254	1742
Passed warm electrical & visual inspections	908	455	232	1595
Resistor & dark SQUID channels excluded	861	447	213	1521
Detectors appearing in .8 K network analysis	805	430	187	1422
Detectors after SQUID failures removed	773	414	155	1342
Detectors after noise polluters removed	676	371	133	1180
Detectors with successful flight IV curves	504	342	109	955

Table 4.1: The detector yield broken down by observation frequency band, 150, 250, and 410 GHz, as well as the sum. Each row of the table accounts for detector loss.

Table 4.1 provides an accounting of EBEX detector yield as a function of observation

frequency band, as well as the total for the experiment. Each silicon wafer, regardless of observation frequency band, had 140 bolometers and one fabrication alignment mark. The 150 and 250 GHz wafers were coupled to LC boards around the perimeter of the focal plane. These edge LC boards each had 125 readout channels. Because of the alignment mark replacing one bolometer, 124 readout channels were connected to bolometers. The 410 GHz wafers were in the center of each focal plane and had central LC boards offset from the focal plane, in the space just behind the wafer. The central LC boards each had 128 readout channels. Again, because of the alignment mark, 127 readout channels were connected to bolometers. The first two rows of Table 4.1 give the total number of bolometers flown and the total number of bolometers the electronics were capable of reading out.

At room temperature, the wafers were inspected visually and each bolometer was tested for electrical continuity. The visual inspection was done under a microscope and, for example, sometimes revealed incomplete etching evidenced by a column of silicon from the spiderweb to the silicon backing wafer. This was noted as a thermal short and such a detector was not electrically biased. For the electrical inspection, I measured the resistance by either probing directly across the wafer bond pads or by probing the leads on the LC boards. The first method was done in the fabrication clean room and the second method was done after the wafer had been shipped, mounted, and wirebonded to its LC board. The resistance reading was dominated by the room temperature resistance of the niobium leads. The electrical inspection could not identify a short across the TES because the typical room temperature resistance of the TES was a few ohms, much less than the tens of kiloohms of the niobium leads. The electrical inspection did, however, identify which TES or leads did not make a complete electrical connection, i.e. were open. The warm visual and electrical inspection provided an upper limit of the wafer's yield because the open and thermally shorted detectors were guaranteed not to work, third row of Table 4.1.

For flight, each wafer had two bolometers replaced by one ohm resistors near the LC board bond pads. These two channels were dedicated to monitoring read out electronic noise up to the LC board, one channel at a low bias frequency and the other channel at a high bias frequency. Four SQUIDs were not attached to bolometer combs due to opens in the microstrips. These combs were modified to monitor read out electronic

noise up to the SQUID, Table 4.1 row 4.

Upon cooling the wafer, there were wired detector channels which had shown a reasonable room temperature resistance but did not appear in the network analysis, Table 4.1 row 5. Five SQUIDs failed to operate during flight, Table 4.1 row 6. Once a wafer was characterized in a dark cryostat, the detectors which degraded the noise performance of their entire comb were identified and their wirebonds were removed, Table 4.1, row 7.

After EBEX was launched and reached its float altitude, I performed IV curves for all bolometers and the total number of successful curves is reported in Table 4.1, row 8. The losses between row 7 and row 8 were due to detectors being saturated or failing to transition.

4.2 Radiative Load

The IV curve measurements, described in Section 3.1.3, provided the electrical power required to hold the detector in the negative electrothermal feedback regime. In the dark test cryostats, ideally, the radiative load was negligible and so the only power on the detectors was the electrical bias power. That is, for the dark test cryostat IV curve measurements, Equation 2.8 became

$$P_{total} = P_{elec} + \cancel{P_{rad}}, \tag{4.1}$$

I measured P_{elec} dark and that was P_{total}, the total power necessary to hold the detector in the negative electrothermal feedback regime.

Once EBEX reached float altitude and the thick cryostat window was rolled back, IV curves were performed for all detectors. From these IV curves, I measured the electrical power required at float, with the radiative load present, to hold the detector in the negative electrothermal feedback regime. The difference in the two powers measured, in the dark cryostat and open to light at float, gave each detector's measured radiative load,

$$P_{rad} = P_{elec}^{dark} - P_{elec}^{float}, \tag{4.2}$$

Figure 4.1 shows two PV curves for a 250 GHz detector dark in ETC and open to light at float in EBEX.

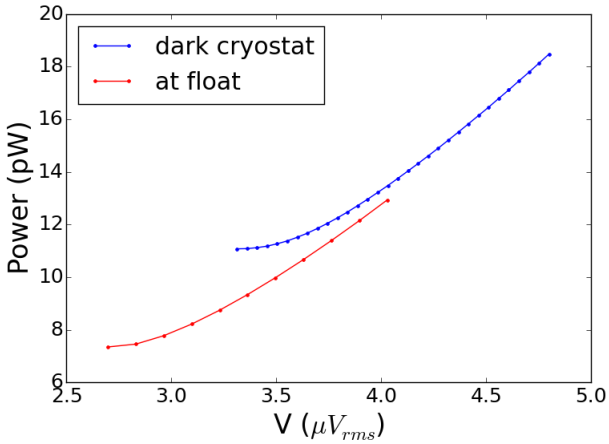

Figure 4.1: Electrical power as a function of bias voltage for a detector from a 250 GHz wafer, dark in ETC (blue) and at float (red). At float, because of the radiative load, less electrical power was required to hold the detector in the negative electrothermal feedback regime. The difference in electrical powers, 4 pW, was the measured radiative load

Figure 4.2 has the distributions of the measured radiative loads from the first set of IV curves performed at float, broken down by observation frequency band. The measured radiative loads were Gaussian-shaped distributions. The Gaussian fits, of 3.6 ± 1.0, 5.3 ± 1.8, and 4.9 ± 1.4 pW, agreed closely with the medians and standard deviations of the distributions, 3.6 ± 1.5, 5.3 ± 1.8, and 5.0 ± 1.4 pW, for 150, 250, and 410 GHz, respectively. There were 37, 9, and 0 detectors at 150, 250, and 410 GHz with negative measured loads. These non-physical measurements were not understood and not included in the radiative load distributions.

The predicted radiative loads were generated by calculating the transmission, reflection, and absorption of each element in the detector's optical path [29]. Assuming detector efficiencies of 0.6, 0.5, and 0.4 at 150, 250, and 410 GHz, the predicted loads were 1.4, 3.7, and 4.7 pW, see Table 2.1. At 250 and 410 GHz, these pre-flight predictions fall within one standard deviation of the measured radiative load. At 150 GHz, the detector efficiency would have to have been 150% in order for the measurement to have matched the predicted load. This unphysical result tells us there was an excess load in the 150 GHz band. Assuming the detector efficiency was actually ~80%, as was

measured in ETC, Section 3.1.4, then the incident power on the 150 GHz bolometers was 4.5 pW, 2.1 pW in excess of the predicted incident power of 2.4 pW.

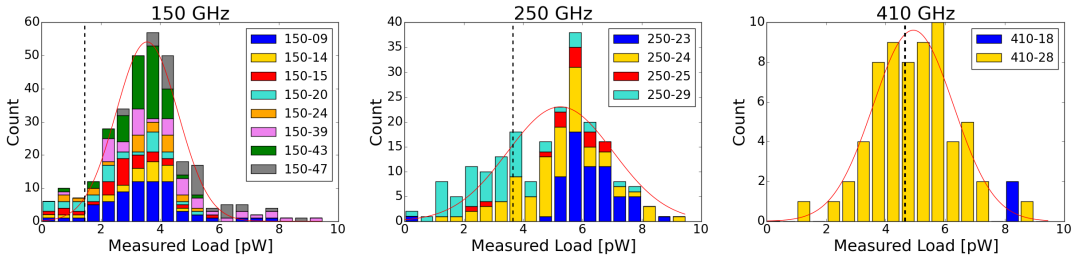

Figure 4.2: Histograms of the measured radiative load from the first detector tuning at float. The different colors represent different wafers. The thin red lines are the gaussian fits of 3.6 ± 1.0, 5.3 ± 1.8, and 4.9 ± 1.4 pW for the 150, 250, and 410 GHz observation bands, respectively. The black dashed vertical lines are the pre-flight predicted loads of 1.4, 3.7, and 4.7 pW, assuming detector efficiencies of 0.6, 0.5, and 0.4, for 150, 250, and 410 GHz.

4.3 In-Flight Noise Performance

The noise performance is assessed by comparing the predicted NEP to the measured NEP. I look at the noise of the dark SQUIDs, the resistor channels, the bolometers over-biased while the stage is cold, and the bolometers dropped into their superconducting transition state.

4.3.1 NEP unit conversions

There are four units I use when measuring the detector NEP: DfMUX ADC counts, Amps, Watts at the detector, and Watts on the sky. The raw timestreams from the DfMUX boards are recorded in ADC counts. The predictions for the current noise terms of the NEP, Johnson and readout, are naturally in units of Amps. The predictions for the power noise terms of the NEP, photon and phonon, are naturally in units of Watts at the detector. To convert to units of power on the sky, I can either use each detector's calibration map of RCW38 or the measured end-to-end instrument efficiency,

$$\varepsilon = \frac{\text{power absorbed by detector}}{\text{incident sky power}} \tag{4.3}$$

Table 4.2 provides the conversion applied to each noise term in order to report in the units of the leftmost column.

Units	Timestream	Photon and Phonon	Johnson and Readout
ct	$\left(\frac{\mathbf{ct}^2}{\mathbf{Hz}}\right)$	$\left(\frac{W_{bolo}^2}{Hz}\right)\left(S_I\right)^2\left(\frac{\mathrm{ct}}{A}\right)^2$	$\left(\frac{A^2}{Hz}\right)\left(\frac{\mathrm{ct}}{A}\right)^2$
A	$\left(\frac{\mathrm{ct}^2}{\mathrm{Hz}}\right)\left(\frac{A}{\mathrm{ct}}\right)^2$	$\left(\frac{W_{bolo}^2}{Hz}\right)\left(S_I\right)^2$	$\left(\frac{\mathbf{A}^2}{\mathbf{Hz}}\right)$
W_{bolo}	$\left(\frac{\mathrm{ct}^2}{\mathrm{Hz}}\right)\left(\frac{A}{\mathrm{ct}}\right)^2\left(\frac{1}{S_I}\right)^2$	$\left(\frac{\mathbf{W}_{bolo}^2}{\mathbf{Hz}}\right)$	$\left(\frac{A^2}{Hz}\right)\left(\frac{1}{S_I}\right)^2$
W_{sky}	$\left(\frac{\mathrm{cts}^2}{\mathrm{Hz}}\right)\left(\frac{W_{sky}}{\mathrm{ct}}\right)^2$	$\left(\frac{W_{bolo}^2}{Hz}\right)\left(S_I\right)^2\left(\frac{\mathrm{ct}}{\mathrm{A}}\right)^2\left(\frac{W_{sky}}{\mathrm{ct}}\right)^2$	$\left(\frac{A^2}{Hz}\right)\left(\frac{\mathrm{ct}}{A}\right)^2\left(\frac{W_{sky}}{\mathrm{ct}}\right)^2$
W_{sky}	$\left(\frac{\mathrm{cts}^2}{\mathrm{Hz}}\right)\left(\frac{A}{\mathrm{ct}}\right)^2\left(\frac{1}{S_I}\right)^2\left(\frac{1}{\varepsilon}\right)^2$	$\left(\frac{W^2}{Hz}\right)\left(\frac{1}{\varepsilon}\right)^2$	$\left(\frac{A^2}{Hz}\right)\left(\frac{1}{S_I}\right)^2\left(\frac{1}{\varepsilon}\right)^2$

Table 4.2: PSD unit conversions used to get all noise terms in the same units. ct is a DfMUX ADC count, W_{bolo} is power absorbed by the detector, S_I is the detector current responsivity, A is current though the SQUID, W_{sky} is power incident from the sky, and ε is the end-to-end instrument optical efficiency.

4.3.2 Procedure

As was done for the ETC noise measurements reported in Section 3.2, the data was broken up into chunks of ∼3 minutes (172 seconds), a gradient and offset were subtracted, a Hann window applied, and the PSD was calculated. The white noise level (WNL) was defined as the square root of the average of the PSD from 3.9 to 4.4 Hz. This is a much narrower band than was used in the dark ETC measurements. It was chosen because part of our signal of interest resided there, in one of the polarization frequency sidebands of 4*f_{HWP} = 4*1.235 Hz = 4.94 Hz.

The following overbiased and in-transition noise analysis looked at the bolometers wired to bolometer readout crates (BRO)s 2, 3, and 4. With the exception of the very first time the bolometers were dropped into their transitions at float and the subsequent half hour of observation, BRO1 was turned off. This was in order to conserve bolometer crate power. The bolometer crate batteries were not charged to their capacity because the gondola motor controller overheated and so the solar panels, responsible for charging the batteries, were not facing the sun as often as was planned. The cost to the overall data acquisition was small because BRO1 happened to be wired to three wafers of bolometers which were largely saturated at float.

Bolometer data, for purposes of noise analysis, were flagged if the detector was

saturated, there were signals from cosmic ray absorption, there were SQUID DC level jumps, the bolometer went superconducting, the half-wave plate (HWP) synchronous signal subtraction failed, the HWP motor was ramping on or off, the cryostat was stepping elevation, or the internal-to-the-cryostat calibrator was on. Flagged data was replaced by white noise realizations. In order for a chunk of data to be included in the noise analysis, I required no more than 10% of the data be flagged. Of the 941 bolometers wired up in BRO2-4, 460 had data which passed the valid criteria.

4.3.3 In-Flight SQUID Noise

In ETC, the SQUID noise performance was measured for SQUIDs with live detectors wired to them but demodulating away from the detector resonant frequencies. In EBEX, however, the SQUID noise performance was measured by dedicated dark SQUIDs. The dark SQUIDs were not attached to any bolometers because there was an open on their microstrips leading from the SQUID boards to the copper pigtails attached to the LC boards. Two SQUIDs were intentionally made dark. Two more microstrip lines opened during the cryostat cooldown effectively creating two more dark SQUIDs. The dark SQUIDs each had 16 demodulators set up from 200 to 1200 kHz. As was done for ETC, the predicted electronic and SQUID noise was calculated from the electronic specifications of each element of the readout chain and assumed an intrinsic SQUID noise of 3.5 $pA/\sqrt{Hz}$. The measurement in ADC counts was converted to current via the DfMUX transfer functions and compared to the prediction. The left panel of Figure 4.3 is the noise as a function of time for a single dark SQUID channel. The right panel of Figure 4.3 is the distribution of the median measured-to-predicted noise ratio for all of the dark SQUID channels. The data bunched together in the mode on the left are the 48 channels from 3 of the dark squids. All 16 channels of the fourth dark squid showed anomalously high noise throughout flight. The median measured-to-predicted ratio of the distribution on the left was 1.2.

4.3.4 In-Flight Resistor Noise

Each LC board had two bolometers replaced by 1 Ω resistors, one read out at the high end of the demodulation frequencies and the other at the low end. The resistors shared

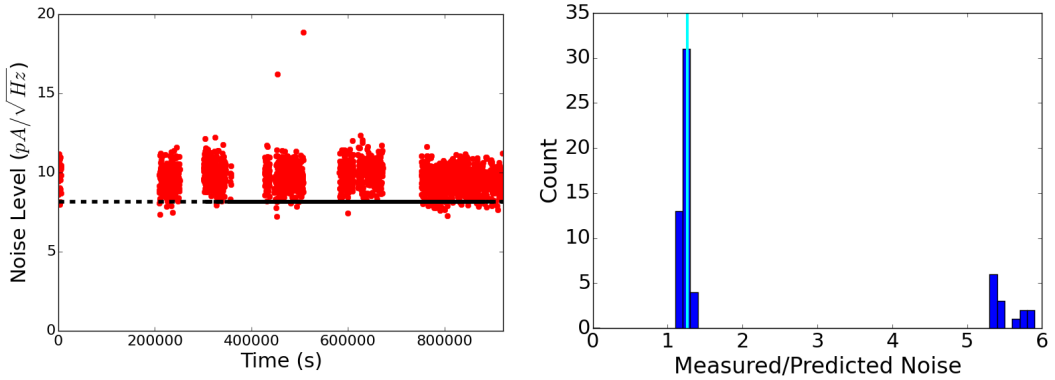

Figure 4.3: Left: the SQUID noise measured (red) and predicted (black) for one dark SQUID channel throughout flight. Right: the distribution of the median measured to predicted noise for all SQUID channels. The median (vertical cyan) of the distribution on the left, the set of well-behaved dark SQUIDs, is 1.2.

the read out chain all the way up to the wafer bond pads of the LC board. Their purpose was to get a handle on the readout (electronic and SQUID) and Johnson noise by excluding the bolometer from the equation and replacing it with a known resistance. The predicted readout noise was calculated as it was for the dark SQUIDs. For the resistors, however, the electronic noise prediction was higher because the carriers and nullers were on in order to more closely mimic the configuration of a real bolometer. The resistance values were taken from the network analysis and the Johnson noise calculated assuming the resistor was well heat sunk to the LC board which was at the bath temperature. The left panel of Figure 4.4 is the measured and predicted noise for one resistor throughout flight. The right panel of Figure 4.4 is the median ratio of measured to predicted noise for 16 of the 21 resistor channels. The median of this distributions was 1.8. The 5 resistors channels with a median measured to predicted noise ratio greater than 6 were excluded from this analysis. Though the bolometer and readout cavity was designed to be RF-tight, we hypothesize the excess noise was due to electromagnetic pickup in the microstrips which were connecting the SQUID boards to the LC boards. The parallel flattened niobium titanium traces, 0.76 mm by 700-950 mm (depending on wire routing restrictions), could have been acting as antennae.

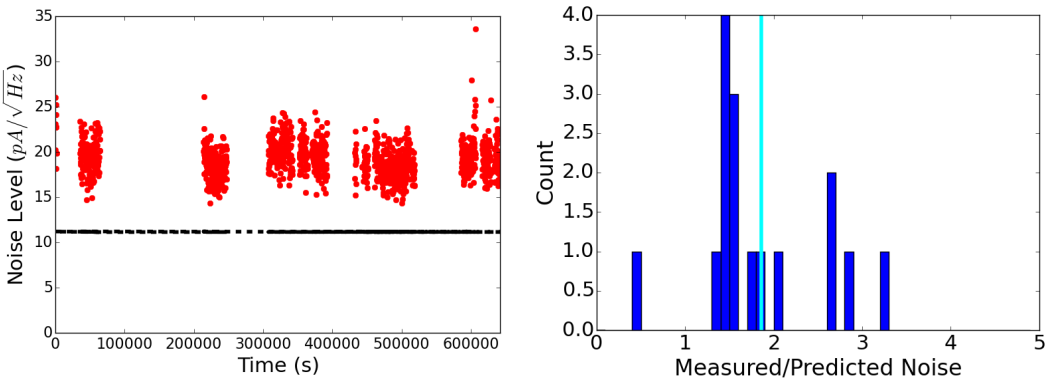

Figure 4.4: Left: the resistor noise measured (red) and predicted (black) for one resistor channel throughout flight. Right: the distribution of the median measured to predicted noise for all resistor channels. The median (vertical cyan) of the distribution is 1.8.

4.3.5 In-Flight Bolometer Overbiased Noise

A detector was said to be overbiased when the voltage bias across the TES provided enough Joule heating to keep the resistance of the TES normal. Because of the small value of the loopgain when the bolometer was overbiased, the responsivity was tiny and so the noise performance was dominated by the readout (electronic and SQUID) and bolometer Johnson noise, Equation 2.17. I predicted and measured the bolometers' overbiased noise in units of $A/\sqrt{Hz}$ since both the readout and Johnson noise are naturally in units of current. The readout noise was calculated as before, using each bolometer's carrier and nuller settings. The predicted Johnson noise assumed the bolometer resistance was R_{normal} from the network analysis fit and estimated the bolometer temperature as $T_{bolo} = T_c + \Delta P/\overline{G}$, where T_c was measured dark, ΔP was the difference in power overbiased to in the transition from the flight pv curve, and $\overline{G}$ was measured dark and corrected for the EBEX bath temperature. Because the bolometers and resistors shared the readout chain all the way to just before the bolometer wafer, I assumed the excess noise present in the resistor channels would also be present in the bolometer channels. The predicted overbias noise for each bolometer was multiplied by 1.8, the median factor of excess noise measured by the resistors. The prediction, including the excess factor from the resistor measurements, was calculated for each bolometer and

Table 4.3 reports the median overbiased noise prediction for each wafer in $pA/\sqrt{Hz}$.

The left panel of Figure 4.5 shows the measured and predicted overbiased noise for one 150 GHz bolometer. At float, the bolometers were in their overbiased state after the fridge cycle, but while the focal planes were still cooling to their base temperatures. The right panel of Figure 4.5 is the measured and predicted noise every 172 seconds over a ∼6000 second time period while the focal planes were cooling the last 50 mK to their base temperatures. I took the median ratio of the measured to predicted overbiased noise over this 6000 second interval as representative of the bolometer's overbiased noise performance. Figure 4.6 is the median measured to predicted overbiased noise ratio for each bolometer. The median ratio of of all detectors was 1.2. The majority of the detectors have a coherency value of ∼0.1, indicating the excess noise is not from a correlated noise source but rather is a broadband source. The median ratio per wafer is reported in Table 4.3. Note, wafers 150-20, 150-24, 250-25, and 410-18 were not included in the table because they were either in BRO1 (off) or saturated.

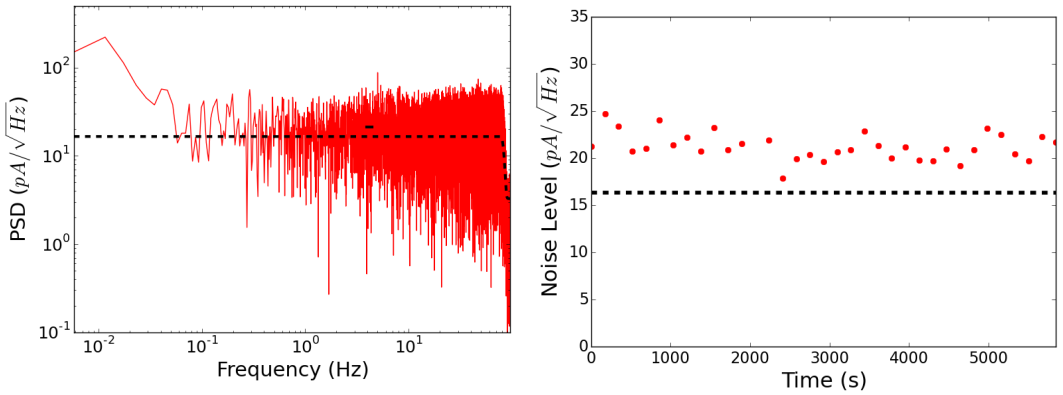

Figure 4.5: Left: the current spectral density of one 150 GHz detector during one 172 s section of the flight when it was overbiased (solid red) and the predicted quadrature sum of the Johnson and readout noise (dashed black). We quote noise levels averaged over a narrow band from 3.9 to 4.4 Hz (thick solid black). Right: the measured to predicted readout and Johnson noise ratio as a function of time for the same detector.

Figure 4.7 is a plot of the ratio of the overbiased noise prediction to the measurement as a function of the bias frequency. Around 1 MHz, there is a slight but systematic increase in the measured noise. This was not understood.

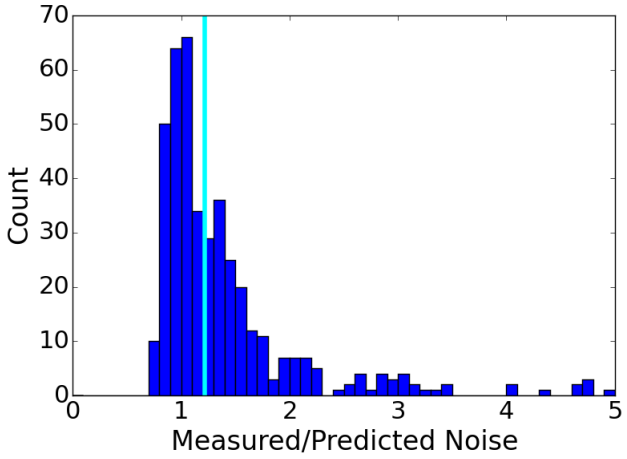

Figure 4.6: Histogram of the median ratio of measured to predicted readout and Johnson noise for all bolometers. The prediction for each bolometer has been multiplied by 1.8, the median factor of excess noise measured by the resistor channels. There are 34 bolometers with a ratio greater than 5. The median value (vertical cyan) is 1.2.

Wafer	Prediction ($pA/\sqrt{Hz}$)	Measured Ratio
150-09	18	1.1
150-14	17	1.1
150-15	16	1.2
150-39	19	1.5
150-43	19	1.1
150-47	21	1.1
250-23	19	1.0
250-24	21	1.3
250-29	18	1.4
410-28	24	1.4

Table 4.3: The predicted combination of Johnson and readout noise for each wafer. The theoretical predictions have been boosted by a factor of 1.8, the excess of noise measured by the resistors. For each wafer the measaured to predicted ratio quoted is the median of the distribution for the detectors on that wafer.

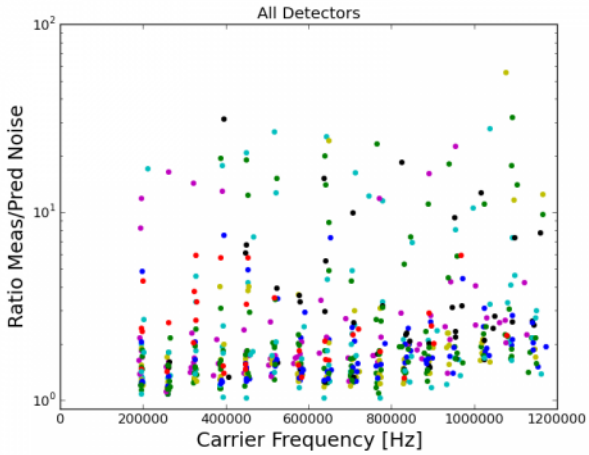

Figure 4.7: Overbias measured to predicted noise ratio as a function of bolometer bias frequency. There is a slight increase in the noise measured for bolometers around a bias frequency of 1 MHz.

4.3.6 In-Flight In-Transition Noise Prediction

I predicted the in-transition NEP in $aW/\sqrt{Hz}$ at the detector. The in-transition noise included the readout, Johnson, phonon, and photon noise, Equation 2.17. In order to report the data in units of power at the detector, the readout and Johnson noise, as well as the measured counts from the detector timestream, were divided by the bolometer current responsivity, see Table 4.2 for unit conversions. I assumed we were in the high loopgain regime so $S_I \sim \sqrt{2}/V_{bias}$.

The phonon NEP contribution was estimated assuming the detector temperature was T_c and calculating the thermal conductance as described in Equation 3.8. In order to estimate the photon NEP contribution at float, I took P_{rad} to be the radiative load measured by each detector, Section 4.2. The center and width of the observation frequency bands, ν (153, 244, and 393 GHz) and $\Delta\nu$ (25, 28, and 45 GHz), were from calibration measurements of the EBEX spectral response on the ground [26]. I did not have a measure of the photon correlation noise factor, so I assumed it was completely correlated, $\xi = 1$. This put an upper bound on the noise prediction and had the greatest effect on the 150 GHz NEP prediction. For the 150 GHz band, if the photons were completely uncorrelated, $\xi = 0$, then the photon NEP in $W/\sqrt{Hz}$ would have

decreased by a factor of 0.80, decreasing the total NEP prediction by a factor of 0.90. For the 410 GHz band, the decrease in photon NEP would have been a factor of 0.95, decreasing the total NEP prediction by a factor of 0.98.

Figure 4.8 is a stacked bar chart of the EBEX in-transition noise prediction per wafer in units of aW/$\sqrt{Hz}$ at the detector. Each wafer's bar was the mean for that wafer and the error bars were one standard deviation. The dark blue bar was the predicted NEP using the preflight expected radiative load, Table 2.1, to calculate the photon noise contribution and using each detector's carrier and nuller settings as well as its dark characterization measurements to calculate the readout, Johnson, and phonon noise contributions. The cyan bar included the additional NEP given the *measured* radiative load of each detector. The golden bar included the excess factor of 1.8, measured on the resistor channels, applied to the bolometer readout and Johnson noise.

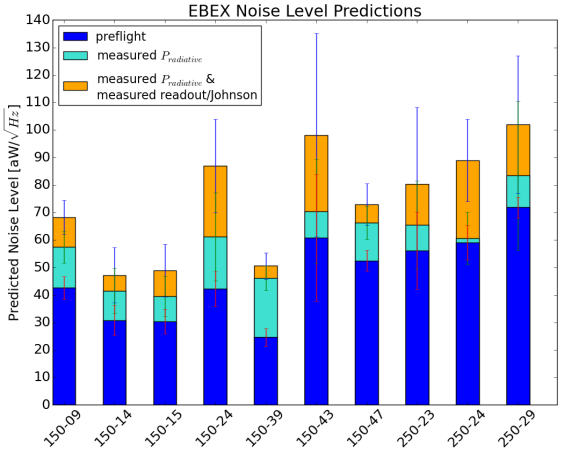

Figure 4.8: The EBEX pre-flight NEP prediction (blue), including the measured radiative load (cyan), and including the boost to readout and Johnson noise (gold).

Figure 4.9 gives the breakdown of the noise components per observation frequency band as pie charts in units of aW^2/Hz. Both the readout and Johnson noise include the excess factor of 1.8 measured by the resistors. The bolometer sensitivity floor was designed to be dominated by the photon noise. The excess measured in the electronic, readout, and Johnson noise terms, however, brought the expected readout noise to a level comparable to that of the expected photon noise. The median predicted in-transition

NEP level broken down by wafer is reported in Table 4.4.

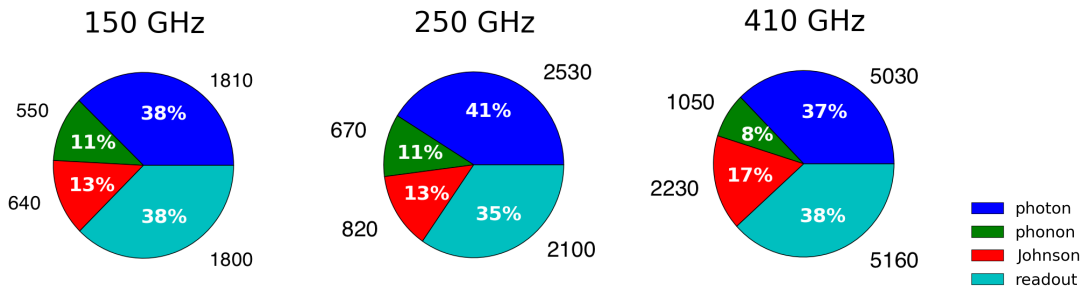

Figure 4.9: Individual components of the NEP prediction in aW^2/Hz per band. The readout and Johnson NEP terms include the excess factor of 1.8 measured with the resistor channels and with the detectors overbiased.

4.3.7 In-Flight In-Transition Noise Measurement

The HWP was spinning during the in-transition noise measurements. There was a large HWP synchronous signal in the raw timestream I subtracted in order to be able to extract the WNL. Figure 4.10 is the square root of the PSD of a 172 second chunk of time with the HWP synchronous signal present (red) and subtracted (gold) for a detector on wafer 150-09. Just as for the other noise measurements, the measured WNL, indicated by the short thick black line, was the square root of the average of the PSD between 3.9 and 4.4 Hz. The NEP prediction, indicated by the thin black dashed line, was calculated as described in Section 4.3.6.

For approximately ten minutes at float, the bolometers were biased into their transitions and the HWP was *not* spinning. Figure 4.11 compares the median WNL from the ten minutes with the HWP stationary to the median WNL from the ten minutes after the HWP was turned back on. There was a median increase of 8 $aW/\sqrt{Hz}$ in the NEP when the HWP was on compared to when it was off. Coupling of the HWP rotation mechanism noise to the readout electronics could be the source of the increase in measured NEP when the HWP was on.

The top panel of Figure 4.12 is the measured and predicted NEP for one 150 GHz bolometer throughout flight. The prediction changed as a function of time because the measured radiative load changed and also the detector bias parameters (carrier

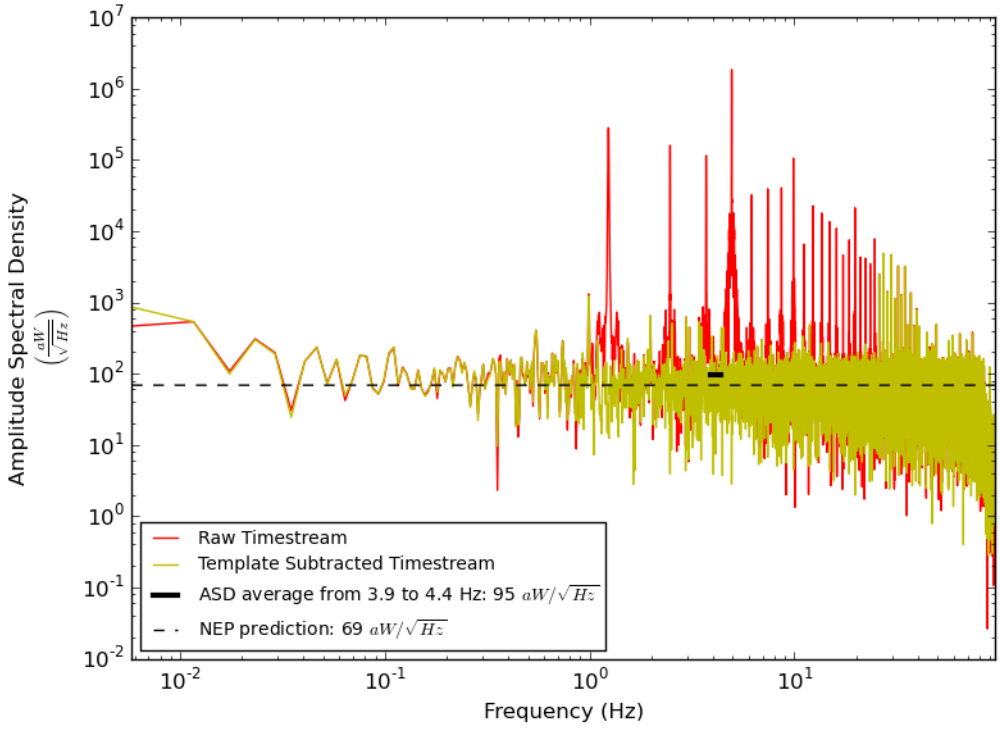

Figure 4.10: In-transition noise for a ∼3 minute chunk of time from a 150 GHz bolometer with the HWP template present (red) and subtracted (gold).

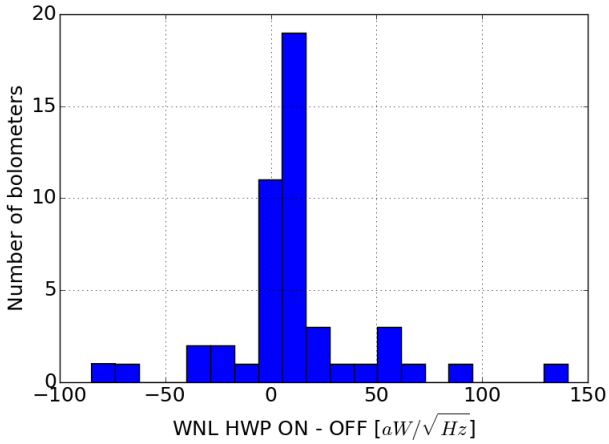

Figure 4.11: Histogram of the difference between the median NEP measured with the HWP on and off.

and nuller settings) changed with each tuning. The bottom panel of Figure 4.12 is a histogram of the ratio of the measured to predicted noise at each point. Though there sometimes seemed to be systematic noise differences from observation to observation, the median value of the histogram was taken as representative of each bolometer's noise performance throughout flight. Each wafer's median measured to predicted NEP ratio is reported Table 4.4.

A histogram of the median of each detector's measured to predicted in-transition noise throughout flight is shown in Figure 4.13. Taking into account the excess over-biased noise factor of 1.8 in the readout and Johnson noise terms and using each detector's measured radiative load, the measured NEP agreed with the predictions to within one standard deviation. The breakdown by wafer is reported in Table 4.4

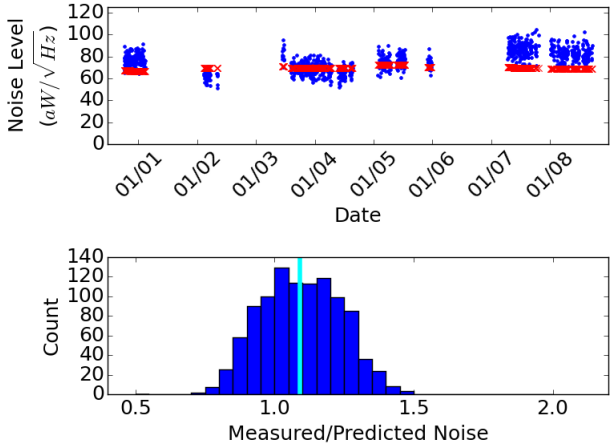

Figure 4.12: Top: In-transition measured (blue dots) and predicted (red crosses) NEP for one bolometer on wafer 150-09 throughout flight. The readout and Johnson noise terms of the prediction have been boosted by the excess noise factor of 1.8 measured by resistor channels. Gaps in time indicate times data is absent or has been rejected. Bottom: The distribution of the measured to predicted NEP ratio for this detector throughout flight. The median ratio (vertical cyan) is 1.1.

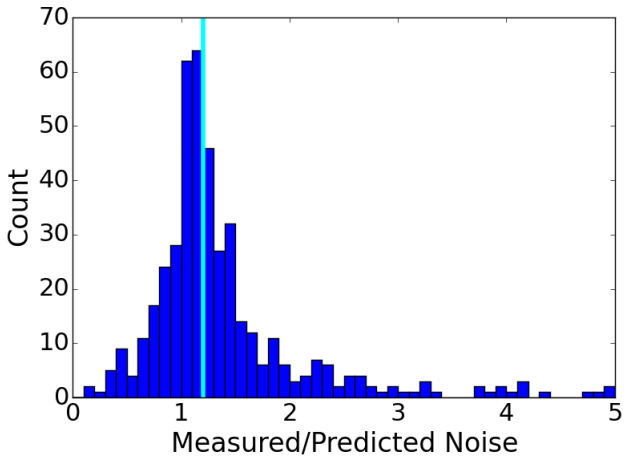

Figure 4.13: The distribution of the median ratio of measured to predicted in-transition noise throughout flight for all bolometers. The predicted noise includes the boost factor of 1.8 to the readout and Johnson noise terms measured by the resistor channels. The median ratio (vertical cyan) is 1.2.

Wafer	Predicted NEP [aW/$\sqrt{\text{Hz}}$]	Measured/Predicted NEP
150-09	68	1.1
150-14	45	0.8
150-15	47	1.2
150-39	77	1.1
150-43	56	1.1
150-47	59	1.4
250-23	80	1.1
250-24	76	1.4
250-29	93	1.5
410-28	110	1.6
All Detectors		1.2

Table 4.4: The median predicted NEP and measured-to-predicted NEP ratio for each wafer and combined for all detectors. The readout and Johnson noise terms of the prediction include the excess factor of 1.8 measured by the resistor channels.

Chapter 5

Conclusion

To measure the tiny polarization signal of the CMB, EBEX employed a kilopixel array of TES bolometers. In order to realize the benefits of the space-like environment in which EBEX flew, I worked with our collaborators at Berkeley to optimize the detectors for the lower, more stable radiative load at float. That meant modifying detector parameters such as their normal resistances, transition temperatures, thermal conductances, and time constants. I measured detector parameters for each of the flight wafers, as well as more than two dozen wafers which didn't fly. Table 2.2 summarizes the design and median measured values of the detector parameters for the flight wafers. Chapter 3 discusses the measurements. The results of the measurements tended to be grouped by fabrication run, i.e. by wafer. For some wafers, we were able to achieve our design parameters.

The sensitivity of the detectors was quantified by their NEP. I used the characterization measurements to predict the NEP. In the dark ETC, I was able to achieve the predicted NEP for the readout electronics and for the detectors in an overbiased state. Biased at 90% of their normal resistance, I was able to get measured noise within 5% of the prediction. Once the detectors were dropped deep into their transitions, however, the measured noise diverged from the prediction. I suspect the detectors started to become unstable and oscillate, increasing the measured noise. For flight, I operated the detectors at 85% of their normal resistances. The SQUID noise at float was 20% higher than predicted, and the electronic and Johnson noise measured by 1 Ω resistors was 80% higher than predicted. When predicting the NEP for the detectors, I assumed the

detectors' electronic and Johnson noise was also a factor of 1.8 greater than the original prediction. With this assumption, the median ratio of measured to predicted overbiased NEP for all detectors open to light was 1.2. The median ratio of measured to predicted in-transition NEP for all detectors open to light was also 1.2. The source of the excess noise is not understood.

References

[1] A. H. Guth. Inflationary universe: a possible solution to the horizon and flatness problems. *Physical Review D*, 23:347–356, jan 1981.

[2] A. Linde. A new inflationary universe scenario: A possible solution of the horizon, flatness, homogeneity, isotropy and primordial monopole problems. *Phys Lett B*, 108:389, 1982.

[3] P.J.E. Peebles. *Principles of Physical Cosmology*. Princeton University Press, 1993.

[4] D.N. Spergel et al. Three-year wilkinson microwave anisotropy probe (wmap) observations: Implications for cosmology. *Astrophysical Journal Supplement*, 170:377–408, jun 2007.

[5] M. Tegmark et al. Cosmological constraints from the sdss luminous red galaxies. *Physical Review D*, 75:123507, 2006.

[6] Planck Collaboration. Planck 2015 results. xiii. cosmological parameters. *Astronomy & Astrophysics*, 594:A13, sep 2016.

[7] Planck Collaboration. Planck 2015 results. xx. constraints on inflation. *Astronomy & Astrophysics*, 594:A20, sep 2016.

[8] E. M. Leitch et al. Degree angular scale interferometer 3 year cosmic microwave background polarization results. *Astrophysical Journal*, 624:10–20, may 2005.

[9] T. E. Montroy et al. Measurement of the cmb ee spectrum from the 2003 flight of boomerang. *Astrophysical Journal*, 647:813–822, aug 2006.

[10] J. H. P. Wu et al. Maxipol: Data analysis and results. *Astrophysical Journal*, 665:55–66, aug 2007.

[11] J. L. Sievers et al. Implications of the cosmic background imager polarization data. *Astrophysical Journal*, 660:976–987, may 2007.

[12] M. R. Nolta et al. Five-year wilkinson microwave anisotropy probe observations: Angular power spectra. *Astrophysical Journal Supplement*, 180:296–305, feb 2009.

[13] L. P. Grishchuk. Amplification of gravitational waves in an istropic universe. *Sov Phys JETP*, 40:409–415, 1975.

[14] A. A. Starobinsky. Dynamic of phase transition in the new inflationary universe scenario and generation of perturbations. *Phys Lett B*, B117:175–178, 1982.

[15] M. V. Rubakov, V. A. Sazhin and A. V. Veryaskin. Graviton creation in the inflationary universe and the grand unification scale. *Phys Lett B*, 115:189–192, sep 1982.

[16] A. A. Starobinskii. The perturbation spectrum evolving from a nonsingular initially de- sitter cosmology and the microwave background anisotropy. *Soviet Astronomy Letters*, 9:302–304, jun 1983.

[17] L. F. Abbott and M. B. Wise. Constraints on generalized inflationary cosmologies. *Nuclear Physics B*, 244:541–548, 1984.

[18] K. N. Abazajian et al. Inflation physics from the cosmic microwave background and large scale structure. *Astroparticle Physics*, 63:5565, March 2015.

[19] Planck Collaboration. Planck intermediate results. xxx. the angular power spectrum of polarized dust emission at intermediate and high galactic latitudes. *Astronomy and Astrophysics*, 586(A133), feb 2016.

[20] The POLARBEAR Collaboration. A measurement of the cosmic microwave background b- mode polarization power spectrum at sub-degree scales with polarbear. *Astrophysical Journal*, 794:171, 2014.

[21] S. Naess et al. The atacama cosmology telescope: Cmb polarization at 200 <l <9000. *Journal of Cosmology and Astroparticle Physics*, oct 2014.

[22] R. Keisler et al. Measurements of sub-degree b-mode polarization in the cosmic microwave background from 100 square degrees of sptpol data. *Astrophysical Journal*, 807, jul 2015.

[23] Planck Collaboration BICEP2/Keck. Planck intermediate results. xxx. the angular power spectrum of polarized dust emission at intermediate and high galactic latitudes. *Physical Review Letters*, 114:101301, 2015.

[24] Chaoyun Bao. *Foreground Cleaning for Cosmic Microwave Background Polarimeters in the Presence of Instrumental Effects*. PhD thesis, University of Minnesota, 2015.

[25] The EBEX Collaboration. EBEX Paper 3. *Astrophysical Journal*, 2016.

[26] Kyle Zilic. *Calibration and Design of the E and B EXperiment (EBEX) Cryogenic Receiver*. PhD thesis, University of Minnesota, 2014.

[27] K. Zilic, A. Aboobaker, F. Aubin, C. Geach, S. Hanany, N. Jarosik, M. Milligan, and I. Sagiv. A Double Vacuum Window Mechanism for Space-borne Applications. *Review of Scientific Instruments*, 88(4):045112, April 2017, 1702.01861.

[28] The EBEX Collaboration. EBEX Paper 1. *Astrophysical Journal*, 2016.

[29] The EBEX Collaboration. EBEX Paper 2. *Astrophysical Journal*, 2017.

[30] John E. Ruhl et al. The south pole telescope. In *Millimeter and Submillimeter Detectors for Astronomy II*, volume 5498 of *Proc. SPIE*, page 11, 2004.

[31] D. Schwan et al. Millimeter-wave bolometer array receiver for the atacama pathfinder experiment sunyaev-zeldovich (apex-sz) instrument. *Review of Scientific Instruments*, 82:091301, 2011, 1008.0342.

[32] S.P. Langley. *The bolometer*. The Society, New York, 1881.

[33] M. Tinkham. *Introduction to Superconductivity*. McGraw-Hill, NY, 2 edition, 1996.

[34] P L Richards. Bolometers for Infrared and Millimeter Waves. *Journal of Applied Physics*, 76:1–24, 1994.

[35] Shih-fu Lee, Jan M Gildemeister, Warren Holmes, Adrian T Lee, and Paul L Richards. Voltage-biased superconducting transition-edge bolometer with strong electrothermal feedback operated at 370 mK. *Applied optics*, 37(16):3391–3397, 1998.

[36] J C Mather. Bolometer noise: nonequilibrium theory. *Applied Optics*, 21(6):1125–1129, 1982.

[37] J. B. Johnson. Thermal agitation of electricity in conductors. *Phys. Rev.*, 32:97–109, Jul 1928.

[38] J. M. Lamarre. Photon noise in photometric instruments at far-infrared and submillimeter wavelengths. *Applied Optics*, 25(6), Mar 1986.

[39] Benjamin G. Westbrook. *Studies of the Cosmos Using Spiderweb Absorber Transition Edge Sensor Bolomters*. PhD thesis, University of California, Berkeley, 2014.

[40] Irwin K. Hilton G. Transition-edge sensors. In *Cryogenic Particle Detection*, volume 99. Springer, Berlin, Heidelberg, 2005.

[41] K. D. Irwin, G. C. Hilton, D. A. Wollman, and J. M. Martinis. Thermal-response time of superconducting transition-edge microcalorimeters. *J. Appl. Phys.*, 83:3978, 1998.

[42] M. A. Dobbs et al. Frequency Multiplexed SQUID Readout of Large Bolometer Arrays for Cosmic Microwave Background Measurements. *Review of Scientific Instruments*, page 28, December 2011.

[43] Johannes Hubmayr. *Bolometric detectors for EBEX : a balloon-borne cosmic microwave background polarimeter*. PhD thesis, University of Minnesota, 2009.

[44] J. B. Peterson and P. L. Richards. A Cryogenic Blackbody for Millimeter Wavelengths. *International Journal of Infrared and Millimeter Waves*, 5(12):1507–1515, December 1984.

[45] Aubin Francois. *Detector readout electronics for EBEX : a balloon-borne cosmic microwave background polarimeter*. PhD thesis, McGill University, 2012.

[46] Martin E Huber, Patricia A Neil, Robert G Benson, Deborah A Burns, Alan M Corey, Christopher S Flynn, Yevgeniya Kitaygorodskaya, Omid Massihzadeh, and John M Martinis. DC SQUID Series Array Amplifiers with 120 MHz Bandwidth. *IEEE Transactions on Applied Superconductivity*, I(I), 2001.